



Simultaneous Multiwavelength Flare Observations of EV Lacertae

Rishi R. Paudel^{1,2}, Thomas Barclay^{3,2}, Joshua E. Schlieder³, Elisa V. Quintana³, Emily A. Gilbert^{3,4,5,6},
Laura D. Vega^{1,3,7,8,16}, Allison Youngblood⁹, Michele L. Silverstein^{3,10,17}, Rachel A. Osten¹¹, Michael A. Tucker^{12,18},
Daniel Huber¹², Aaron Do¹², Kenji Hamaguchi^{2,13}, D. J. Mullan¹⁴, John E. Gizis¹⁴, Teresa A. Monsue^{3,17},
Knicole D. Colón³, Patricia T. Boyd³, James R. A. Davenport¹⁵, and Lucianne Walkowicz⁶

¹ CRESST II and Exoplanets and Stellar Astrophysics Laboratory, NASA/GSFC, Greenbelt, MD 20771, USA

² University of Maryland, Baltimore County, Baltimore, MD 21250, USA; rishi.paudel@nasa.gov

³ NASA Goddard Space Flight Center, Greenbelt, MD 20771, USA

⁴ Department of Astronomy and Astrophysics, University of Chicago, 5640 S. Ellis Ave, Chicago, IL 60637, USA

⁵ University of Maryland, Baltimore County, 1000 Hilltop Circle, Baltimore, MD 21250, USA

⁶ The Adler Planetarium, 1300 South Lakeshore Drive, Chicago, IL 60605, USA

⁷ Department of Astronomy, University of Maryland, College Park, MD 20742, USA

⁸ Vanderbilt University, Department of Physics & Astronomy, 6301 Stevenson Center Ln., Nashville, TN 37235, USA

⁹ Laboratory for Atmospheric and Space Physics, 1234 Innovation Dr, Boulder, CO 80303, USA

¹⁰ RECONS Institute, Chambersburg, PA 17201, USA

¹¹ Space Telescope Science Institute, 3700 San Martin Drive, Baltimore, MD 21218, USA

¹² Institute for Astronomy, University of Hawai'i, 2680 Woodlawn Drive, Honolulu, HI 96822, USA

¹³ CRESST II and X-ray Astrophysics Laboratory NASA/GSFC, Greenbelt, MD, USA

¹⁴ Department of Physics and Astronomy, University of Delaware, Newark, DE 19716, USA

¹⁵ Department of Astronomy, University of Washington, Seattle, WA 98195, USA

Received 2021 April 21; revised 2021 June 28; accepted 2021 July 29; published 2021 November 16

Abstract

We present the first results of our ongoing project conducting simultaneous multiwavelength observations of flares on nearby active M dwarfs. We acquired data of the nearby dM3.5e star EV Lac using five different observatories: NASA's Transiting Exoplanet Survey Satellite (TESS), NASA's Neil Gehrels Swift Observatory (Swift), NASA's Neutron Interior Composition Explorer (NICER), the University of Hawaii 2.2-meter telescope (UH88), and the Las Cumbres Observatory Global Telescope (LCOGT) Network. During the ~ 25 days of TESS observations, we acquired three simultaneous UV/X-ray observations using Swift that total ~ 18 ks, 21 simultaneous epochs totaling ~ 98 ks of X-ray data using NICER, one observation (~ 3 hr) with UH88, and one observation (~ 3 hr) with LCOGT. We identified 56 flares in the TESS light curve with estimated energies in the range $\log E_T$ (erg) = (30.5–33.2), nine flares in the Swift UVM2 light curve with estimated energies in the range $\log E_{UV}$ (erg) = (29.3–31.1), 14 flares in the NICER light curve with estimated minimum energies in the range $\log E_N$ (erg) = (30.5–32.3), and 1 flare in the LCOGT light curve with $\log E_L$ (erg) = 31.6. We find that the flare frequency distributions (FFDs) of TESS and NICER flares have comparable slopes, $\beta_T = -0.67 \pm 0.09$ and $\beta_N = -0.65 \pm 0.19$, and the FFD of UVOT flares has a shallower slope ($\beta_U = -0.38 \pm 0.13$). Furthermore, we do not find conclusive evidence for either the first ionization potential (FIP) or the inverse FIP effect during coronal flares on EV Lac.

Unified Astronomy Thesaurus concepts: Flare stars (540); M dwarf stars (982); Stellar activity (1580)

Supporting material: figure set

1. Introduction

M dwarfs, commonly known as red dwarfs, are the most abundant ($\sim 75\%$) stars in our galaxy (Henry et al. 2006). They are low-mass objects with masses $\lesssim 0.6 M_\odot$ (Burrows et al. 2001) and are considerably cooler and less luminous than the Sun. Due to their convective interiors and rotation, they have relatively strong magnetic fields for their size (Shulyak et al. 2017) and are capable of producing very strong flares with energies up to 10^4 times or greater than the strongest flare observed on the Sun (e.g., Davenport 2016; Osten et al. 2016; Paudel et al. 2018a). It has been shown that M dwarfs of all ages are capable of producing flares (Schmidt et al. 2014; Hawley et al. 1996; Paudel et al. 2018a, 2018b; France et al. 2020).

In the standard picture of a solar flare, energy release is governed by magnetic reconnection in the corona or upper

chromosphere. During a flare, magnetic energy stored in magnetic fields is suddenly released in the form of kinetic energy of particles (ions and electrons), bulk plasma motion, and thermal emission mostly in the form of soft X-rays. Thermal coronal emission (soft X-rays) is produced as a result of heating by the nonthermal electrons produced in the corona. Those electrons also travel along field lines and emit gyrosynchrotron radio emission. Electrons that are accelerated along field lines to the intersections of a magnetic loop with the photosphere produce bremsstrahlung seen in hard X-rays (Schrijver et al. 2016). Flare blackbody (BB) emission is often seen in the UV and optical, sometimes correlating with the steep rise/impulsive phase as seen in X-ray observations (Benz & Güdel 2010). This BB emission is a result of local heating in the chromosphere/photosphere by the particles that precipitate downward after losing their energy in the form of hard X-rays. Kowalski et al. (2013) estimated the typical temperatures of the BB emission to be in the range ~ 9000 – $14,000$ K: at such temperatures, the peak of the spectrum occurs in the near-UV, at wavelengths of order 3000 \AA . The BB radiation escapes from the star in the form of a “white light flare (WLF).”

¹⁶ Heising-Simons Astrophysics Postdoctoral Launch Program Fellow.

¹⁷ NASA Postdoctoral Program Fellow.

¹⁸ DOE CSGF Fellow.

The cumulative flare frequency distribution (FFD) of a flaring star has been found typically to follow a power law. As a result, the FFD can be fit by a linear relation: $\log \tilde{\nu} = C + \beta \log E$, where $\tilde{\nu}$ is the cumulative frequency defined as the number of flares per unit time with energies in excess of E (e.g., Gershberg 2005; Lacy et al. 1976). Each star is observed to have its own particular values of the coefficient C and the spectral index β .

Since M dwarfs commonly host small planets on short-period orbits, M-dwarf planets may be exposed to extreme space weather environments and run the risk of being exposed to the enhanced electromagnetic radiation (mainly X-rays and UV radiation) and energetic particle flux coming from flares. This is particularly important when considering habitability, because M-dwarf HZs are very close to the stars (Kopparapu et al. 2013). For example, the planet Proxima Centauri b receives 30 times more extreme-UV (10–121 nm) flux than Earth, 10 times more far-UV (122–200 nm) flux, and 250 times more X-rays (0.01–10 nm, Ribas et al. 2016). Although certain UV and optical photons from flares can have beneficial effects on life (Ranjan et al. 2017; Mullan & Bais 2018), negative effects of energetic photons and particles are likely to occur. High-energy radiation may have adverse effects on the thermochemical equilibrium of the planets’ atmospheres. This has many consequences, including the loss of surface water, stripping of the planet’s entire atmosphere, or destruction of the ozone layer (Lammer et al. 2007; Segura et al. 2010; Bolmont et al. 2017; Tilley et al. 2019; Chen et al. 2021). To fully account for the impact of M-dwarf flares on exoplanet atmospheres, we must constrain the total energy emitted during the flares on M dwarfs at various wavelengths.

The Transiting Exoplanet Survey Satellite mission (TESS; Ricker 2014) was launched in April 2018 to perform a near-all-sky photometric survey to find small planets around the brightest nearby stars, but also has sensitivity to low-amplitude, short-duration events, like flares. Its photometric bandpass (~600–1000 nm) is more sensitive at redder wavelengths compared to Kepler (Borucki 2017), and combined with its all-sky observing strategy, is ideal for targeting M dwarfs (Ricker 2015; Barclay et al. 2018; Ballard 2019).

Long-baseline, high-precision optical data sets from TESS allow us to observe the diversity of flaring events with amplitudes spanning more than five orders of magnitude. However, atmospheric stripping of planets is caused by the strongly photodissociative UV and X-ray photons, not optical photons (Bolmont et al. 2017). We cannot draw strong conclusions about habitability from optical data alone without first measuring the relationship between X-ray/UV and optical. Large surveys of the high-energy radiation of M dwarfs such as the HST MUSCLES Treasury Survey (France et al. 2016) and HAZMAT (Shkolnik & Barman 2014) have provided detailed UV flaring information on M dwarfs (Loyd et al. 2018a, 2018b), but the link between optical and UV flares remains elusive.

In this paper, we describe the first results from our large program studying nearby active flaring M dwarfs using multiwavelength data sets. We focus on the flaring M dwarf EV Lac, which has been known as a flare star for at least 65 yr (Roques 1955). EV Lac produces flares in the X-ray (e.g., Schmitt 1994; Sciortino et al. 1999; Favata et al. 2000; Huenemoerder et al. 2010), UV (e.g. Ambruster et al. 1986; Pomerance et al. 1995), optical (e.g. Kodaira et al. 1976;

Abdul-Aziz et al. 1995), and radio wavelengths (e.g. White et al. 1989; Abdul-Aziz et al. 1995).

Osten et al. (2005) carried out a simultaneous multi-wavelength observing campaign of EV Lac for two days in 2001 September using radio (VLA), optical (McDonald Observatory), UV (HST), and X-ray (Chandra) telescopes. They observed a large flare at radio wavelengths, two small flares at both optical and UV wavelengths, and at least nine flares in X-ray. A very large flare occurred on this star in April 2008, which resulted in a trigger from Swift’s autonomous gamma-ray burst response (Osten et al. 2010), and is one of the most extreme stellar flares observed in terms of its enhancement relative to the quiescent level. Its peak flux of 5.3×10^{-8} erg cm⁻² s⁻¹ at 0.3–100 keV was estimated to be ~7000 times the star’s quiescent X-ray flux, and in white light the star brightened by ≥ 4.7 mag. At the flare peak, it had $L_X/L_{\text{bol}} \sim 3.1$, where L_{bol} is the bolometric luminosity of the star during the early stages of the flare.

Since EV Lac is nearby and known to produce flares frequently across the electromagnetic spectrum, it is one of the best targets for simultaneous multiwavelength observations.

We observed EV Lac using three space telescopes, TESS, Swift, and NICER, as well as two ground-based telescopes, The University of Hawaii 2.2-meter telescope (UH88) and a one-meter telescope at McDonald Observatory as part of the Las Cumbres Observatory Global Telescope Network (LCOGT; Shporer et al. 2011). In Section 2, we give a brief introduction to EV Lac, and in Section 3, we describe the various observations. Likewise, in Section 4, we present the data reduction and flare analysis. In Section 5, we discuss and summarize the main results of our work.

2. Target Characteristics

EV Lac (GJ 873, LHS 3853), at a distance of only 5.05 pc (Gaia Collaboration et al. 2018a), is one of the most widely studied low-mass stars. In order to measure accurate flare energies, we require a self-consistent set of stellar parameters. We use two methods to estimate the star’s fundamental properties, which include its highly precise Gaia parallax. We used the metallicity-dependent M_{K_s} -radius relationship of Mann et al. (2015) to estimate the stellar radius, adopting $[\text{Fe}/\text{H}] = -0.01 \pm 0.15$ as determined by Rojas-Ayala et al. (2012). To calculate the star’s effective temperature (T_{eff}), we used the relations of Mann et al. (2015) to estimate the K -band bolometric correction, calculated the luminosity, and then substituted luminosity and radius into the Stefan–Boltzmann law. Fundamental parameter uncertainties were estimated via Monte Carlo methods where we adopted Gaussian-distributed measurement errors and added the systematic scatter in each parameter. We estimate $R_* = 0.337 \pm 0.029 R_{\odot}$, $L_* = 0.0124 \pm 0.0007 L_{\odot}$, and $T_{\text{eff}} = 3315 \pm 152$ K. However, in view of the rather large error bars, we consider that it is possible to arrive at more precise values of the parameters of EV Lac by using a different approach as follows.

For comparison, we now turn to the methods of Silverstein et al. (2021, in preparation), which are heavily based on those of Dieterich et al. (2014). To derive effective temperature, we assume $[\text{Fe}/\text{H}] = 0$ and compare an assortment of color combinations from observed Weis (1996) $V_J R_{KC} I_{KC}$, 2MASS JHK_S (Cutri et al. 2003), and WISE All-Sky W1W2W3 (Wright et al. 2010; Cutri et al. 2012) photometry to those extracted from scaled BT-Settl 2011 CIFIST model spectra (Allard et al. 2012). We note that W2 appears brighter by 0.25 mag than W3,

Table 1
Properties of EV Lac

	Value	Units	Ref.
ASTROMETRIC PROPERTIES			
α	$341.7029626 (\pm 0.03 \text{ mas})$	deg	4
δ	$+44.3320170 (\pm 0.03 \text{ mas})$	deg	4
μ_α	-706.1 ± 0.1	mas yr ⁻¹	4
μ_δ	-458.8 ± 0.1	mas yr ⁻¹	4
parallax	198.01 ± 0.04	mas	4
distance	5.049 ± 0.001	pc	15
PHOTOMETRIC PROPERTIES			
V_J	10.22 ± 0.03	mag	11
R_{KC}	9.05 ± 0.03	mag	11
I_{KC}	7.55 ± 0.02	mag	11
J	6.11 ± 0.03	mag	2
H	5.55 ± 0.03	mag	2
K_s	5.30 ± 0.02	mag	2
i	13.215 ± 0.002	mag	3
G	9.000 ± 0.001	mag	4
BP	10.543 ± 0.004	mag	4
RP	7.809 ± 0.001	mag	4
T_{mag}	7.73 ± 0.01	mag	5
W1 ^b	5.241 ± 0.063	mag	12, 13
W2 ^b	4.643 ± 0.042	mag	12, 13
W3 ^b	4.891 ± 0.015	mag	12, 13
PHYSICAL PARAMETERS			
Sp. Type	dM3.5e		1
T_{eff}	3270 ± 80	K	c
M	0.347 ± 0.020	M_\odot	c
R	0.353 ± 0.017	R_\odot	c
L_{bol}	0.0128 ± 0.0003	L_\odot	c
log g	4.89 ± 0.00	log(cm s ⁻²)	5
P_{rot}	4.38	d	8
SPECTRAL PROPERTIES			
[Fe/H]	-0.01 ± 0.15	dex	14
RV	0.19	km s ⁻¹	7
$v \sin i$	3.50	km s ⁻¹	7
ACTIVITY INDICATORS			
EW H α	-4.54 ± 0.04	Å	9
EW Ca II K	14.86	Å	10
log $L_{H\alpha}/L_{\text{bol}}$	-3.76		9
log L_X/L_{bol}	-3.33		6
log R'_{HK}	-4.24 ± 0.11		16

Notes.^a Epoch J2015.5.^b All-Sky Data Release.^c This work.

References: (1) Reid et al. 1995; (2) Cutri et al. 2003; (3) Chambers et al. 2016; (4) Gaia Collaboration et al. 2018a; (5) Stassun et al. 2018; (6) Morin et al. 2008; (7) Reiners et al. 2018; (8) Pettersen 1980; (9) Newton et al. 2017; (10) Youngblood et al. 2017; (11) Weis 1996; (12) Wright et al. 2010; (13) Cutri et al. 2012; (14) Rojas-Ayala et al. 2012; (15) Bailer-Jones et al. 2018; (16) Melbourne et al. 2020.

and both W1 and W2 bands are affected by saturation; we suspect the excess in W2 is saturation-induced, rather than from an infrared source such as a circumstellar disk. We believe the impact of potentially underestimated W1 and W2 magnitudes is likely negligible in our analysis because these bands are far into the Rayleigh–Jeans tail. Repeating the procedure 16 times, with permutations of W1 and/or W2 values varied by +0.1, +0.2, or +0.3 magnitudes, yielded effective temperature values ranging from 3270 to 3340 K,

equal to or within the error bars of our adopted value of 3270 ± 80 K. Once an effective temperature is derived, we iteratively modify the model spectrum closest to our results using a polynomial scaling factor until the observed and new model photometry match to within 0.063 mag. This 0.063 value corresponds to the largest error bar in our observed photometry. We integrate the resulting spectrum across the wavelength range of our observed photometry and apply a bolometric correction based on the amount of flux expected in the remaining wavelengths of a BB of the same temperature. We scale the final flux by the Gaia DR2 parallax (Gaia Collaboration et al. 2018a) to calculate bolometric luminosity and derive a radius using the Stefan–Boltzmann Law. Varying W1 and W2 as described earlier yields only a small range of luminosity values ($0.0125\text{--}0.0130 L_\odot$) and radius values ($0.340\text{--}0.353 R_\odot$), on the order of our error bars. We estimate $R_* = 0.353 \pm 0.017 R_\odot$, $L_* = 0.0128 \pm 0.0003 L_\odot$ ($\log_{10} L_* = -1.894 \pm 0.011$), and $T_{\text{eff}} = 3270 \pm 80$ K. We also estimate the mass of EV Lac using the M_K –mass relation of Benedict et al. (2016) and find $0.347 \pm 0.020 M_\odot$. These stellar parameters are consistent with those estimated using the Mann et al. (2015) relations. We adopt these parameters for EV Lac and list them in Table 1. We also use the scaled model spectrum derived using the methods detailed here in our white light flare analysis presented in Section 4.

We compile these properties, additional properties, and their literature references in Table 1. The star’s mass, radius, and spectral type of dM3.5e place it close to, but later than, the range of spectral types (dM2e–dM3e) where main-sequence stars are believed to make a transition between partially convective and fully convective interiors (Houdebine et al. 2017). This fully convective structure in EV Lac, along with its rotation period of ~ 4.4 days, results in strong magnetic activity. Previous observations provided constraints on the star’s magnetic fields, revealing they cover $>50\%$ of the stellar surface and have strengths of ≈ 4 kG (Saar 1994; Johns-Krull & Valenti 1996). This magnetic activity manifests itself in the form of star spots, flares, and associated high-energy emission. Observationally, EV Lac is found to be the second brightest X-ray source seen in the *ROSAT* All-Sky Survey (Hünsch et al. 1999).

2.1. Stellar Age

Aspects of EV Lac’s high level of magnetic activity may also be traced to its age. Here, we investigate multiple properties of the star that in aggregate provide an age constraint in order to study the star’s flare properties in the context of other targets in the “M Dwarf Flares Through Time” program.¹⁹

HR Diagram Position—The slow evolution of low-mass stars like EV Lac as they contract to the main sequence provides the means to estimate ages via position on the Hertzsprung–Russell Diagram (HRD). Assuming similar metallicities, younger M dwarfs appear brighter than older stars. The advent of precision Gaia parallaxes and photometry allows for comparisons of EV Lac’s HRD position to similar stars in populations with well-determined ages. We use EV Lac’s Gaia parallax and photometry (Gaia Collaboration et al. 2018a) to calculate its absolute magnitude ($M_G = 10.484$) and color ($BP - RP = 2.735$) in the Gaia bands, and compare its HRD position to populations of low-mass stars of known age presented in Gaia Collaboration et al. (2018b). EV Lac

¹⁹ TESS Guest Investigator programs G011266 and G022252, PI J. Schlieder, and G03226, PI M. Silverstein.

is ≈ 0.4 mag fainter than the majority of similar color stars in the ~ 110 – 125 Myr old Pleiades cluster (Stauffer et al. 1998; Dahm 2015), and has a similar absolute magnitude when compared to low-mass stars in the ~ 600 – 800 Myr old Praesepe (Brandt & Huang 2015a; Douglas et al. 2017) and Hyades (Brandt & Huang 2015b; Douglas et al. 2019) clusters. These comparisons suggest an age of >125 Myr for EV Lac, but do not provide a stringent limit.

X-ray Emission—We use EV Lac’s measured ROSAT count rate and hardness ratios from the 2RXS catalog of Boller et al. (2016) and the count rate to flux conversion from Schmitt et al. (1995) to calculate an X-ray flux of 4.13×10^{-11} erg cm $^{-2}$ s $^{-1}$. We then combined this with the Gaia DR2 stellar distance to estimate an X-ray luminosity of 1.27×10^{29} erg s $^{-1}$. We compared this luminosity with the X-ray properties of the young to old populations presented in Bowler et al. (2012). Comparing to Bowler et al. (2012), their Figure 5, EV Lac has an X-ray luminosity that matches the Pleiades cluster distribution within 1σ of the median and matches the Hyades cluster distribution within 2σ of the median. In the same Bowler et al. (2012) figure, EV Lac’s X-ray luminosity is more than $250\times$ larger than the median luminosity of old low-mass stars in the galactic field.

Rotation—EV Lac is a relatively rapid rotator, with $P_{\text{rot}} = 4.38$ days measured via periodic brightness modulations in SUPERWASP photometry (Pollacco et al. 2006). This rotation period is consistent with the period we estimate using the TESS photometry (see Section 4). In the period–color diagrams presented in Curtis et al. (2020), this rotation period places EV Lac among other M dwarfs in Praesepe, but also close to the slowest rotators in the Pleiades. As an additional constraint, we also use EV Lac’s rotation period and the M-dwarf rotation–age relation of Engle & Guinan (2018) to estimate an age of 280^{+220}_{-230} Myr, consistent with the general range of ages inferred from other diagnostics.

Kinematics—Using probabilistic methods to study membership in stellar kinematic groups, Klutsch et al. (2014) suggest EV Lac may be a member of the Ursa Major moving group (UMaG; Proctor 1869; Roman 1949; King et al. 2003), which would indicate an age of ≈ 400 Myr (Jones et al. 2015). However, Shkolnik et al. (2012) do not associate EV Lac with any of the moving groups they study, including UMaG. We use the star’s updated Gaia astrometry to calculate its galactic velocities and compare to the revised Ursa Major group properties presented in Gagné et al. (2018). Following the methods of Johnson & Soderblom (1987), we calculate $(UVW)_{\text{EV Lac}} = (+19.765, +3.596, -1.709) \pm (0.004, 0.002, 0.002)$ km s $^{-1}$. For the UMaG, Gagné et al. (2018) report $(UVW)_{\text{UMaG}} = (+14.8, +1.8, -10.2)$ km s $^{-1}$. EV Lac’s galactic velocities are broadly consistent with the UMaG in U and V , but it is a significant outlier in W . The star’s galactic position is also removed from the core of the UMaG group, lying ~ 20 pc away from the tightly clustered nucleus described by Mamajek (2010) and Schlieder et al. (2016). We do note that EV Lac’s kinematics place the star among the proposed UMaG stream members proposed by King et al. (2003), but the membership of many of these stars remains unconfirmed. As a final check, we use BANYAN Σ (Gagné et al. 2018), a Bayesian analysis tool that estimates the probability of kinematic group membership. BANYAN Σ suggests that EV Lac is not a kinematic member of the UMaG (0% probability) or any other group included in the analysis. The star’s kinematics are broadly consistent with other young stars in the solar neighborhood, but group membership cannot be confirmed.

Age Summary—In aggregate, the available observations and calibrated samples for comparison indicate that EV Lac is an intermediate-age M dwarf. Its HR Diagram position indicates it is likely older than the ~ 125 Myr Pleiades cluster, while its X-ray luminosity and rotation rate suggest an age comparable to the 600–800 Myr Hyades and Praesepe clusters and perhaps younger. The star’s galactic velocities and positions are also broadly consistent with proposed members of the ~ 400 Myr UMaG kinematic stream, but its membership remains inconclusive. Given these properties, we quantitatively place EV Lac in the 125–800 Myr age range.

3. Data Sets

3.1. TESS

TESS observed EV Lac (TIC 154101678, GJ 873, 2MASS J22464980+4420030) during Sector 16 (2019 September 11–2019 October 07) as a part of its Cycle 2 observations. EV Lac was observed in two-minute cadence as a part of proposals G022252, G022198, G022080, and G022056. The total TESS observation time is 23.2 days. We used the SAP flux for our analysis after filtering using the ‘hard’ bitmask option in the data analysis tool “Lightkurve” (Vinícius et al. 2018) and removing NaNs from the data.

3.2. Swift/XRT Data

EV Lac was observed by Swift’s X-ray telescope (XRT; Burrows et al. 2005) three times on 2019 September 21–22, via the mission’s Target of Opportunity (ToO) program (#12734 and #12758). The XRT is mainly designed to observe soft X-rays in the energy range of 0.3–10 keV using CCD detectors and has an energy resolution of ≈ 140 eV in the region of the Fe K-line at $E = 6.4$ keV. The first observation occurred on 2019 September 21 at UT 12:34:57 for a time interval of 7.1 ks, the second on 2019 September 22 at UT 11:02:32 for 8.0 ks, and the third on 2019 September 23 at UT 13:51:18 for 2.9 ks. The observing IDs for the three observations are 00031397002, 00031397003, and 00031397004, respectively.

The star was observed in Photon Counting (PC) mode, as well as Windowed Timing (WT) mode for very short intervals. WT mode is preferred whenever the count rate is very high, thereby causing saturation in CCD detectors in the PC mode. Since no major events occurred on the star during the Swift observations, we analyzed the data collected in PC mode only. We obtained the raw data from UK Swift Science Data Centre (UKSSDC). We used Swift XRTPIPELINE task (version 0.13.5) and calibration files from the High Energy Astrophysics Science Archive Research Center (HEASARC)’s calibration database system (CALDB; index version = “x20190910”) to reduce the raw data and produce cleaned and calibrated files. We obtained the X-ray light curve using HEASARC’s XSELECT, a high-level command interface for the HEASARC FTOOLS, to extract a circular region of radius 30 pixels centered at the position of the source (R.A. = $341^{\circ}70$, decl. = $+44^{\circ}33$). A 30 pixel radius circle encloses $\sim 95\%$ of the PSF for a bright source.²⁰ We found that the average photon count rate is 0.40 counts s $^{-1}$ for the quiescent level,²¹ so the pileup correction was not applied. The pileup generally occurs

²⁰ https://www.swift.ac.uk/analysis/xrt/files/xrt_swguide_v1_2.pdf

²¹ The enhanced X-ray events were excluded while estimating the quiescent level.

when the count rate is high ($\gtrsim 0.5$ counts $^{-1}$),²² such that multiple photons registered in a given CCD detector have overlapping charge distributions. This may result in an incorrect classification of a true X-ray event. We used only grade 0–12 events in the PC mode, which are considered to be good for science.

We used the BARYCORR²³ FTOOL to perform barycenter correction on our XRT data, and XSELECT to extract source and background spectra from the cleaned event list. For this, the same circular extraction region described above was used for the source. For the background, we used an annular extraction region with inner radius of 40 pixels and outer radius of 70 pixels centered at the source position. The exposure maps were prepared while running XRTPipeline using option `createexpomap=yes`, and the ancillary response file (ARF) was produced using XRTMKARF, which needs an XRT response matrix file (RMF). We used v014 RMF: `swxpc0to12s6_20130101v014.RMF` obtained from the CALDB file.

3.3. Swift/UVOT Data

The Swift Ultra-Violet/Optical Telescope (UVOT; Roming et al. 2005) also observed EV Lac during the same time as the XRT. The first observation started on 21 September at UT 12:34:55, the second on 22 September at UT 11:02:29, and the third on 23 September at UT 13:51:20. All three observations were performed with the UVM2 filter centered at $\lambda = 2259.84$ Å ($\lambda_{\min} = 1699.08$ Å, $\lambda_{\max} = 2964.30$ Å, FWHM = 527.13 Å). The raw data were obtained from UDSSDC, and then processed in two steps to obtain a cleaned event list. First, we used COORDINATOR²⁴ to convert raw coordinates to detector and sky coordinates. Second, we used UVOTSCREEN to filter the hot pixels and obtain a cleaned event list.

A calibrated light curve was extracted from the cleaned event list by using the FTOOL UVOTEVTLC. For the source, we used the recommended circular extraction region of radius of 5'' around the source position, and for a smooth background, a circular extraction region of radius 30'' away from source. Furthermore, we used `timebinalg=u` to bin time by 11.033 s. It is required that the bin size be a multiple of the minimum time resolution of UVOT data, which is 11.033 ms. UVOTEVTLC applies a coincidence loss correction whenever there is pileup of photons on detectors, by using the necessary parameters from CALDB. After this, the light curve was barycenter corrected by using BARYCORR. To place all the observations on a common time system, the barycentric times were then converted to the Modified Julian Date (MJD) system.

3.4. Neutron Star Interior Composition Explorer (NICER)

During TESS Sector 16, EV Lac was observed simultaneously by NASA’s NICER X-ray mission (Gendreau et al. 2016), via the ToO program. NICER was designed to study soft X-rays within the energy band 0.2–12 keV, with high signal-to-noise ratio photon-counting capability. It has an X-ray Timing Instrument with time-tagging resolution of <300 nsec (absolute), which is much better than other current X-ray

missions (e.g., 100–1000 times better than XMM). Its energy resolution is similar to those of the XMM and Chandra non-grating CCD instruments (137 at 6 keV).

NICER observed EV Lac on 21 different days for a total exposure time of ~ 98 ks (Observation IDs: 21004201[25–45]). We obtained calibrated and cleaned event files of our observation from the NICER archive.²⁵ The cleaned event files were obtained from raw data using the NICER-specific HEASoft tool NICERDAS.²⁶ They were barycenter corrected by using BARYCORR. We then used XSELECT to generate light curves. For the spectral analysis, we applied the latest calibration (ver. 20200722) to the unfiltered event data and processed the data through the standard screening criteria using the `nicer12` FTOOL. NICER does not provide spatial information regarding the source, but it does provide timing and energy information for each photon. Therefore, it is not possible to extract light curves nor spectra by using source and background extraction regions. However, the mission provides background estimator tools to estimate the background spectra. We used the `nibackgen3C50` (v6) tool for extracting source spectra and estimating background spectra of the corresponding time intervals. This tool uses a background events file that was created from “blank sky” observations by NICER. The “blank sky” region was based on the Rossi X-ray Timing Explorer background fields. Detectors 14 and 34 are known to suffer from increased noise. Thus, we excluded data from those detectors and used the `g2020a` background model to generate background spectra. We produced detector response (`rmf` and `arf`) files for these spectra, by following the instruction at section “Calculating ARF and RMF for Different Subset of Modules” in https://heasarc.gsfc.nasa.gov/docs/nicer/analysis_threads/arf-rmf/.

3.5. University of Hawaii 2.2-meter (UH88) Telescope

We were awarded two nights to observe EV Lac with the SNIFS instrument (Lantz et al. 2004) on the University of Hawaii 2.2-meter telescope (UH88) at Maunakea Observatories, 2019 September 20 and 2019 September 21. SNIFS has two modules, a blue arm and a red arm, which combine to cover a broad wavelength range. The blue arm covers 320–560 nm with a resolving power ~ 1000 at 430 nm. The red arm covers and 520–1000 nm with a resolving power ~ 1300 at 760 nm.

On September 20, the humidity was above allowable limits and we were unable to open. On September 21, we obtained 10 spectra of EV Lac with 90 s exposures and 11 with 30 s exposures. These spectra showed significant variability due to variable cloud coverage throughout the night, and the last few exposures were completely contaminated by clouds.

Due to the limited amount of time with no clouds and low enough humidity, we only obtained ~ 3 hr worth of monitoring data of EV Lac. Therefore, the time series spectra were not useful for flare monitoring. During the period we were observing, there was at least one small (<.5%) white light flare visible in the TESS photometric light curve. However, due to cloud variability, we were unable to discern any visible evidence of this flare in the spectra.

²² <https://www.swift.ac.uk/analysis/xrt/pileup.php>

²³ <https://heasarc.gsfc.nasa.gov/ftools/caldb/help/barycorr.html>

²⁴ <https://heasarc.nasa.gov/ftools/caldb/help/coordinator.html>

²⁵ https://heasarc.gsfc.nasa.gov/docs/nicer/nicer_archive.html

²⁶ https://heasarc.gsfc.nasa.gov/docs/nicer/data_analysis/nicer_analysis_guide.html

The spectra were reduced using the SNIFS reduction pipeline (Bacon et al. 2001) and flux calibrated using archival photometry. We used the Buton et al. (2013) model to correct for atmospheric attenuation. We then confirmed the flux calibration by using Gaia data (Zacharias et al. 2013; Tonry et al. 2018). We examined one of our spectra with minimal impact from cloud cover (see Figure 1) and confirm it is consistent with the previously estimated M3.5 spectral type of EV Lac. The spectrum also exhibits emission in several activity diagnostic lines, like H α , as previously observed.

3.6. Las Cumbres Observatory (LCOGT)

EV Lac was observed by the LCOGT 1 m network on 2019 September 17, 2019 September 21, and 2019 September 23 as part of program NOAO2019B-001. We used 30 s exposures in the Bessell-U filter and obtained useful data over a period of ~ 3 hr. Observations on 2019 September 21 were limited by weather, and 1.5 hr of useful photometry were collected each on 2019 September 17 and 2019 September 23. We used LCOGT’s reduced images from the automatic pipeline software BANZAI, which performs bad-pixel masking, bias subtraction, dark subtraction, and flat-field correction, and applies an astrometric solution (McCully et al. 2018). We extracted aperture photometry of EV Lac and eight comparison stars using Photutils, an Astropy package for detection and photometry of astronomical sources (Bradley et al. 2016). We observed one distinct flare and the slow decay of at least one other flare.

In Table 2, we list the dates when EV Lac was observed by a given facility and the corresponding total observation time. The observation times of various facilities are also highlighted in the upper plot of Figure 2. Each of the flares observed simultaneously by TESS and other facilities are given TESS IDs, which are shown above each flare in the figure except for flare T7. T5 is a small-amplitude flare that cannot be seen in this figure.

From here onward, unless otherwise mentioned, the times are expressed in terms of TESS time, which is BJD–2457000 (days) for all the facilities.

4. Analysis

4.1. White Light Flares Observed by TESS

We conducted a white light flare analysis for EV Lac using one sector of TESS two-minute cadence data. Following the methods of Pitkin et al. (2014), we pulled the light curve from the Mikulski Archive for Space Telescopes using `lightkurve`. We then used an adapted version of `bayesflare` on the TESS data to detect stellar flares using Bayesian inference. The routine `bayesflare` uses a sliding window to inspect all of the data points by comparing them to a flare template and determining the odds that the data are described best by a flare with noise or just noise. Using this method, we identified 56 flares in the TESS light curve.

This flare detection routine returns the basic flare parameters we require to model the flares. We also used a Lomb–Scargle periodogram (LSP) to estimate a rotation period; see Figure 3. We then simultaneously model the smoothly varying light-curve modulations caused by star spots and flares simultaneously. We built the model using a framework of `PyMC3` (Salvatier et al. 2016), `celerite` (Foreman-Mackey et al. 2017; Foreman-Mackey 2018), and `xoflares` (Barclay & Gilbert 2020). We use a

periodic Gaussian Process (GP) to model the starspot-modulated stellar rotation using a “Rotation term” from `celerite`, and long-term variability (with a jitter term to capture white noise) in the light curve. The LSP rotation period is used as a prior in this model. At the same time, we use the flare properties from `bayesflare`—full width at half maximum (FWHM), peak time, and peak amplitude—to seed the flare model and sample the flare properties using `xoflares` (Barclay & Gilbert 2020). We sampled over the posterior of our flare model to map the posterior distribution. We did this using `PyMC3`’s Automatic Differentiation Variational Inference algorithm (Kucukelbir et al. 2016) with 100,000 iterations and drawing 3000 samples from the posterior distribution. We included as a model parameter the integral of each flare, which allowed us to determine posteriors on the flare energies.

In Figure 4, we show the TESS light curve in the top panel with the GP fit to the rotational modulation in green. We detrend the GP model from the data and show the flare model overlaid in pink in the middle panel. In the bottom panel, we plot the residuals obtained after subtracting both the GP and flare models from the light curve. The flare parameters obtained after GP modeling are listed in Table 3. The first column is the flare ID, the second is the flare peak time, the third is the FWHM, the fourth is the amplitude, the fifth column is the equivalent duration (ED), and the sixth column is the flare energy.

We used the modified model spectrum resulting from our spectral energy distribution analysis described in Section 2 to determine precise flare energies, as the UH88 spectrum did not cover the full TESS bandpass (Figure 1 top panel). The model matches both the UH88 spectrum and VRIJ photometry, which probe portions of the wavelengths covered by the TESS bandpass. We multiplied the model spectrum by the TESS transmission function to determine the energy emitted by EV Lac within the TESS bandpass (Figure 1 bottom panel). We then integrated across the whole wavelength range, and found the flux ($\text{erg s}^{-1} \text{cm}^{-2}$) emitted by a quiescent EV Lac in the TESS band to be $F_{\text{ref}} = 2.68 \times 10^{-9} \text{ erg s}^{-1} \text{cm}^{-2}$. We scaled this with the distance (d) to EV Lac and calculated the energy per flare as follows:

$$E_{\text{abs}} = \int_{t_0}^{t_1} A(t) dt * F_{\text{ref}} * 4\pi d^2, \quad (1)$$

where A is the modeled flux of the light curve. The estimated energy E_T of each flare in the TESS band is listed in the last column of Table 3. We determined 1σ uncertainties for each flare from our sampling, described above. The white light FFD of EV Lac observed by TESS is shown in Figure 5.

4.2. Swift/XRT

The Swift XRT light curve is shown in Figure 6. We constructed the light curve using `XSELECT`, and present it with a time binning of 120 s. We see a rise in X-rays at $t \sim 1749.3$ days. A flare is also seen in the TESS data right after this observation, but there is no direct overlap. We cannot confirm if the rise is due to a flare. In order to estimate the quiescent X-ray flux of the star, we used `XSPEC v12.10.1f` (Arnaud 1996), an X-ray Spectral Fitting Package developed by HEASARC²⁷ for spectral fitting.

To prepare a spectrum for fitting, we used `GRPPHA` to bin the XRT spectrum of the source obtained by using `XSELECT` to have at least 20 counts per bin, a necessary condition to use

²⁷ See <https://heasarc.gsfc.nasa.gov/xanadu/xspec/>.

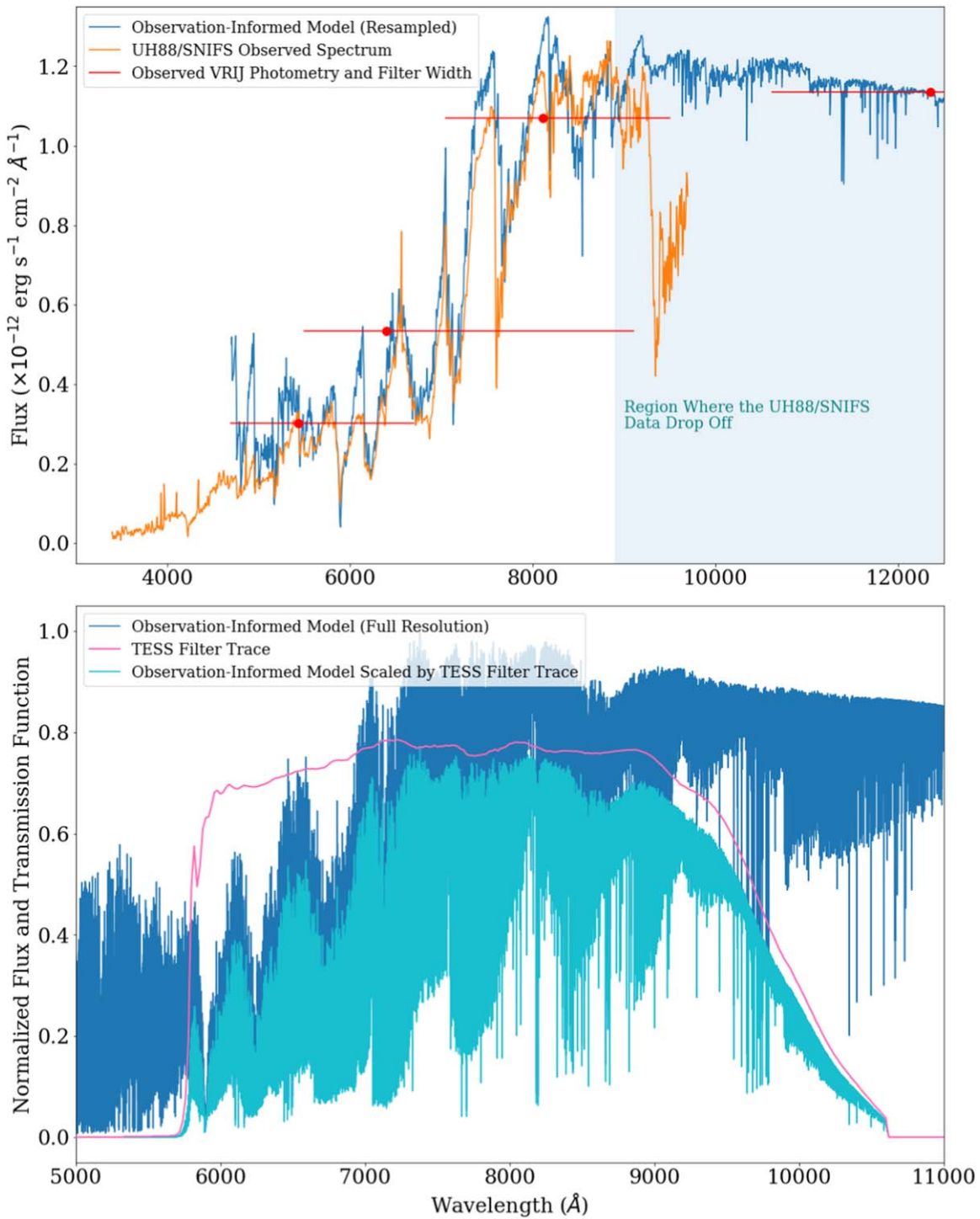


Figure 1. Top Panel: The flux calibrated spectrum of EV Lac taken with UH88/SNIFS (orange) shows emission and absorption lines consistent with an active M dwarf. The observation-informed model spectrum (blue) described in Section 4 resampled to the UH88/SNIFS resolution and the photometry used to derive it (in that wavelength window, red) are overlaid to show the match between both spectra and the photometry. The points and lines correspond to the effective wavelength and width of each filter, respectively. The shaded region demonstrates where the UH88/SNIFS data drop off in quality and then end completely. Because the model spans the full wavelength range of the TESS filter and matches observations, we adopt it for our analysis in Section 4. Bottom Panel: We multiplied the observation-informed model spectrum (blue) described in Section 4 with the TESS transmission function (pink) in order to determine the total energy emitted by EV Lac within the TESS bandpass.

χ^2 statistics (Yamada et al. 2019). We used the two-discrete temperature ($2T$) VAPEC (Smith et al. 2001) model to fit the observed spectrum. A correction due to column absorption was considered while fitting using $N_H = 4.0 \times 10^{18} \text{ cm}^{-2}$. The fitted temperatures are $T_1 = 5.0_{-0.6}^{+1.0} \text{ MK}$ and $T_2 = 20.0_{-5.2}^{+7.5} \text{ MK}$, and

the corresponding volume emission measures (VEM) are $1.5_{-0.6}^{+0.6} \times 10^{51} \text{ cm}^{-3}$ and $0.9_{-0.3}^{+0.3} \times 10^{51} \text{ cm}^{-3}$, respectively. Using this model, we estimate the quiescent X-ray flux of EV Lac to be $1.0 \times 10^{-11} \text{ erg cm}^{-2} \text{ s}^{-1}$ in the 0.3–2.0 keV energy band (soft X-rays).

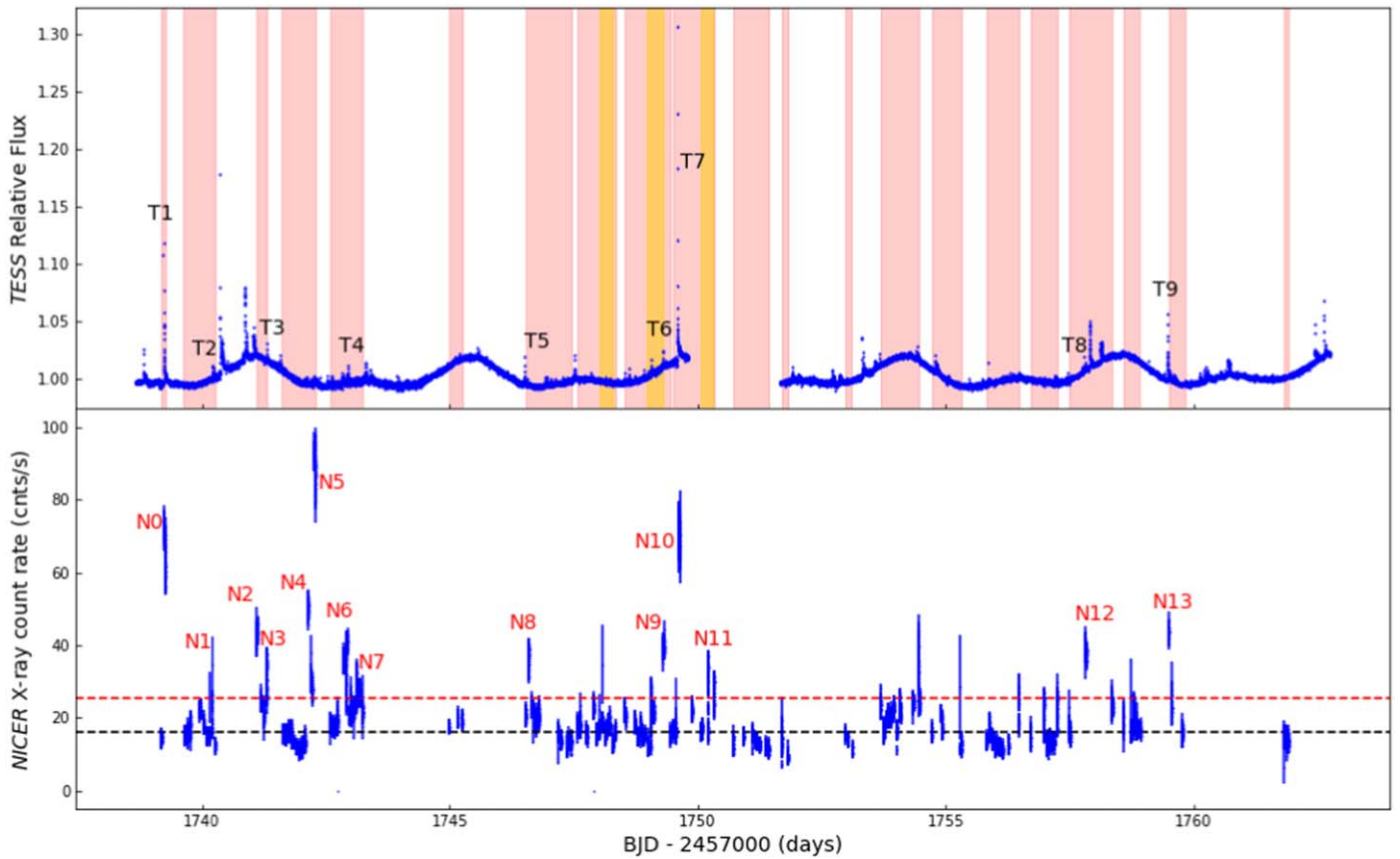


Figure 2. Upper Panel: The EV Lac light curve obtained by TESS during Sector 16. Pink shaded regions correspond to times when the star was observed by NICER, and the orange shaded regions correspond to times when it was observed by Swift. The IDs T1 through T9 represent the flares observed simultaneously by TESS and other facilities. These flare IDs are also listed in Table 3. Lower Panel: NICER X-ray light curve of EV Lac. We identify 14 flares in this light curve (labeled N0 through N13), but none were observed for their full duration. Some events have single-point brightening or are due to background signal. The black dashed horizontal line corresponds to the quiescent level (M_N), and the red dashed line corresponds to $M_N + 2.5\sigma$ value of count rate, which we also consider as a threshold for identifying flares in this light curve.

Table 2
Summary of Observation Times

Facility	Date of obs.	Time observed
TESS	2019 Sep 11–Oct 07	~25 days
Swift XRT	2019 Sep 21–23	18 ks
Swift UVOT	2019 Sep 21–23	18 ks
NICER	2019 Sep 12–Oct 05	97.7 ks
UH88	2019 Sep 20–21	~3 hr
LCOGT	2019 Sep 17–23	~3 hr

We used the $2T$ VAPEC model to fit the spectrum of event observed in between $t = 1749.2$ and 1749.3 days, during which we observed an increase in X-rays. The count rate is $0.76 \text{ counts s}^{-1}$. Therefore, we applied pileup correction before extracting the spectrum. The fitted temperatures are $T_1 = 3.9^{+1.3}_{-1.0}$ MK and $T_2 = 20.9^{+12.8}_{-4.1}$ MK, and the corresponding VEM are $2.8^{+1.8}_{-0.9} \times 10^{51} \text{ cm}^{-3}$ and $3.4^{+0.9}_{-0.9} \times 10^{51} \text{ cm}^{-3}$, respectively. We estimate the flux corresponding to this event to be $1.9 \times 10^{-11} \text{ erg cm}^{-2} \text{ s}^{-1}$ in the 0.3–2.0 keV energy band.

4.3. Swift/UVOT

The Swift UVM2 light curve obtained by using the cleaned event list is shown in Figure 7 with a time binning of 11.033 s.

The median count rate in the light curve is $6.3 \text{ counts s}^{-1}$ and corresponds to the quiescent level for the UVM2 filter. We identified nine flares in this light curve. Two flares were observed on 2019 September 21, five on 2019 September 22, and two on 2019 September 23. The full durations of three flares extend beyond the durations of our observations. Hence, they were only partially observed. One started at $t = 1748.2379$ days, the next started at $t = 1749.2952$ days, and another was observed only during its decay phase on $t = 1750.21$ days.

We converted the count rate in the UVM2 filter to flux in units of $\text{erg cm}^{-2} \text{ s}^{-1} \text{ \AA}^{-1}$ by using an average count rate to flux conversion ratio of 8.446×10^{-16} . The conversion ratio is part of the Swift UVOT CALDB and was obtained using GRB models.²⁸ Using this conversion ratio and the FWHM ($\Delta_{\text{uv}} = 530 \text{ \AA}$) of the UVM2 filter, we found the quiescent UVM2 flux to be $2.8 \times 10^{-12} \text{ erg cm}^{-2} \text{ s}^{-1}$.

The detailed morphologies of the individual flares identified in the UVOT light curve are shown in Figure 8 with a time binning of 11.033 s. The flux plotted along the Y-axis of each plot is the relative flux obtained by dividing the flux by the median flux. Likewise, the time plotted along the X-axis of each plot is centered at T_0 , which is the TESS time at which a given flare started. To compute the flare energies, we first

²⁸ https://heasarc.gsfc.nasa.gov/docs/heasarc/caldb/swift/docs/uvot/uvot_caldb_counttofluxratio_10wa.pdf

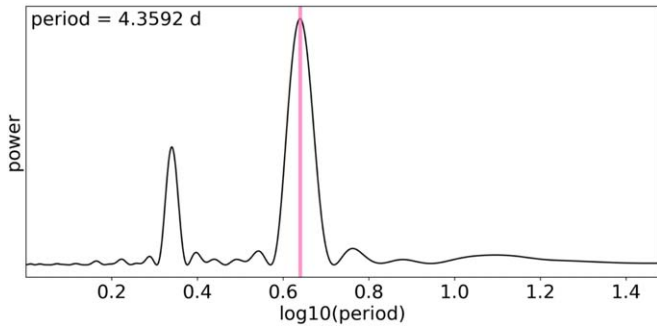


Figure 3. Lomb–Scargle periodogram of the TESS light curve, revealing a prominent peak at the rotation period of EV Lac, which we determine to be 4.3592 days.

estimated the ED of each flare, which is the time during which the flare produces same the amount of energy as the star does when it is in its quiescent state (Gershberg 1972). The flare energies E_f were then computed by:

$$E_f = ED \times 4\pi d_*^2 \times F_q, \quad (2)$$

where d_* is the distance to the star and F_q is the quiescent flux in units of $\text{erg cm}^{-2} \text{s}^{-1}$. In Table 4, we list the estimated energies of all flares, along with their start times, stop times, and EDs. A lower limit on the flare energy is given for each of the three flares that were not observed for their full durations.

4.4. NICER

We show the light curve of EV Lac obtained by NICER in the lower plot of Figure 2. The median count rate of the light curve is $M_N = 16.0 \text{ counts s}^{-1}$, and the standard deviation is $\sigma_N = 3.8 \text{ counts s}^{-1}$. To obtain these parameters, we first excluded any large events with $>25 \text{ counts s}^{-1}$ after an initial inspection of the light curve, ensuring only the large flare-like events were excluded and almost all the quiescent state of the star was included. We then used a threshold cutoff value of $M_N + 2.5\sigma_N$ to identify flares in the light curve. We identify 14 flares, but none of them were observed for their full duration. In the lower panel of Figure 2, each flare is given an ID consisting of the letter “N” followed by a number. The black dashed line corresponds to M_N , and the red dashed line corresponds to $M_N + 2.5\sigma_N$. The events that showed only a single point brightening were excluded from our flare sample. There is a flare-like event at $t = 1759.5$ days, but it appears to be due to background noise. This is because there is no flux enhancement in the 0.3–2.0 keV energy band during this event, which is not the case during a flare. We note that there is a very weak indication of a feature that might be due to rotational modulation in the NICER light curve in the lower panel of Figure 2. However, it is not very convincing.

We used XSPEC v12.10.1f for spectral fitting of the flares observed by NICER. Before fitting, we binned the spectra by using GRPPHA. We used the same RMF and ARF described in Section 3.4 during spectral fitting of NICER flares. We used a three-temperature (3T) VAPEC model to fit the spectrum of each flare except for flare N6, together with the abundances of Anders & Grevesse (1989). We used the F-test to compare two-temperature (2T) and three-temperature VAPEC models, and found that the 3T VAPEC model gives a better fit except for flare N6. We applied a correction due to

interstellar absorption to each flare by using a fixed value of column density N_H equal to $4 \times 10^{18} \text{ cm}^{-2}$. A similar value was used by Osten et al. (2005) for this star. The values of fitted parameters are listed in Table 5. We report the errors of fitted parameters at 90% confidence level. A discussion of coronal abundances is deferred to Section 4.10. In Table 5, T_i ($i = 1, 2, 3$) are the fitted flare temperatures, and EM_i ($i = 1, 2, 3$) are the corresponding VEM. Likewise, “F-test prob.” is the probability of the F-test that is used to compare 2T and 3T VAPEC models. A lower probability implies a significant improvement in the fit due to addition of a component in the 2T VAPEC model. The last column “Quies.” corresponds to the fitted values for the quiescent level of the star. The values of flare fluxes are listed in Table 6.

In Figure 9, we show an example of a flare spectrum fitted by using the 3T VAPEC model. The upper panel shows the data and model (solid line), and the lower panel shows the residuals. The spectra of all other flares observed by NICER and the quiescent level are available in the figure set.

We estimated the X-ray energy of each NICER flare by multiplying the flux obtained by fitting each flare by $4\pi d_*^2$ and by the duration of each flare observed by NICER. We list the energies of each flare in Table 6. In this table, the first column is the flare ID, the second column is the flare start time, and the third column gives information about the rise or decay phase of a given flare when it was observed. In the case of five flares, N1, N2, N6, N9, and N13, we only see enhancement in X-ray flux with almost a constant value during the observation.

The fourth column is the X-ray band in which the flare had a significant number of counts. In the fifth, sixth, and seventh columns, we list three different values of duration for each flare: (i) t_N is the total time for which a given flare was observed by NICER, (ii) t_T is the duration of a given flare in TESS data if it was observed simultaneously by TESS, and (iii) $T_{N,\text{gaps}}$ is the total possible duration of a given flare obtained by considering the total time in between two consecutive quiescent levels that were observed by NICER, with flare enhancement in between them.

The energies corresponding to each time duration are given in the last three columns. Since the flares were not observed for their full duration, we can only estimate the maximum and minimum values of energies in terms of duration. Energies corresponding to t_N are the minimum values as they correspond to the energies released during the NICER exposure times of the flares. The energies corresponding to $T_{N,\text{gaps}}$ are the maximum values for a given flare in terms of the flare duration only. The flare energies corresponding to t_N and $T_{N,\text{gaps}}$ are estimated by using the same average flare flux we observed during the flares. We did not use any flare model to estimate these energies, and they do not represent the true values of total energies released during the corresponding flares.

In Table 6, F_f is the average flare flux estimated after subtracting the quiescent flux, and F_f/F_q is the ratio of flare flux to quiescent flux for a given flare. Using the NICER light curve, we estimate the quiescent flux of EV Lac to be equal to $1.3 \times 10^{-11} \text{ erg cm}^{-2} \text{ s}^{-1}$.

4.4.1. Possibility of a Large, Complex X-ray Flare between $t = 1742.10$ and 1742.60 days

NICER observed three enhancements in X-ray flux from EV Lac, in between $t = 1742.10$ and 1742.30 days, which can be seen in Figure 10. We notice a flare decay phase during the

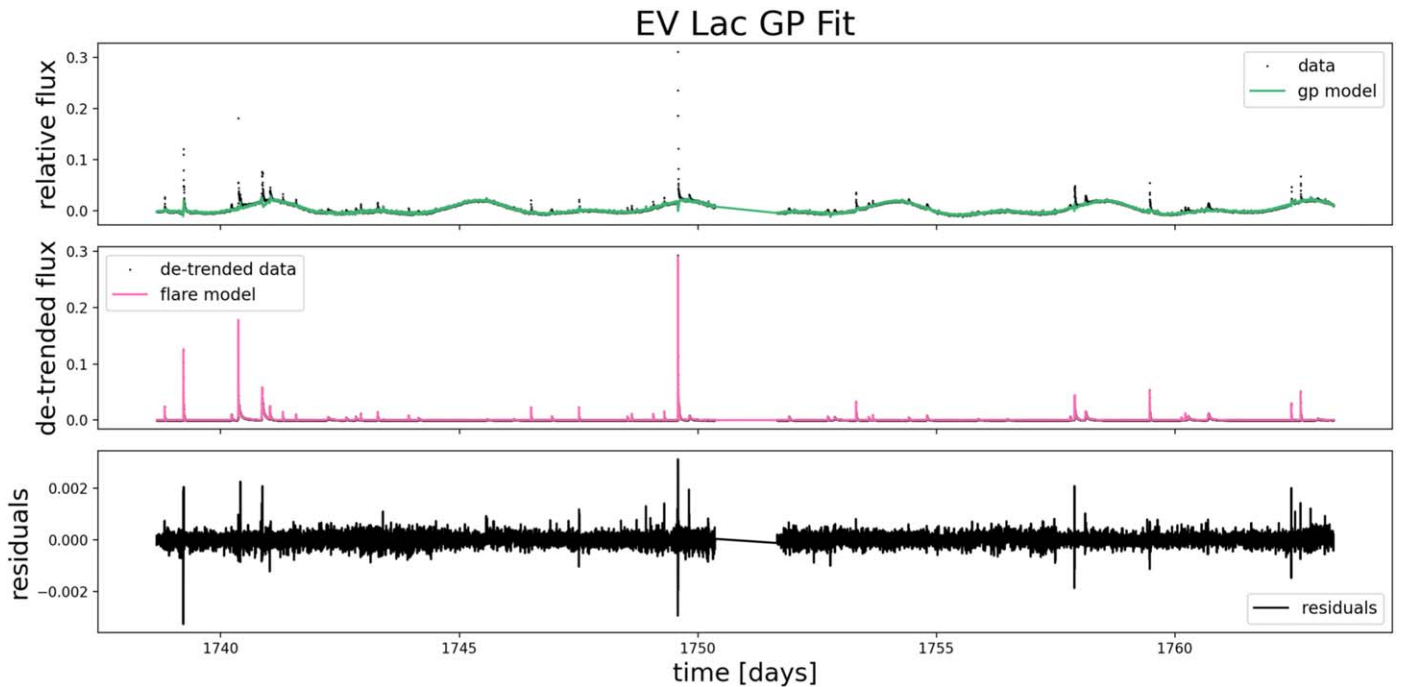


Figure 4. TESS light curve of EV Lac, obtained during Sector 16 (2019 September 11–2019 October 07). The top panel shows the light curve (black) and GP fit of the spot modulation and long-term variability (green). The middle panel shows the detrended light curve after subtracting the GP model, revealing the flares, with the flare model overplotted in pink. The bottom panel shows the residuals obtained after subtracting both the GP and flare models from the light curve. Our flare analysis identifies 56 EV Lac flares during the 23.2 days covered by the TESS light curve.

enhancement at $t = 1742.20$ days, so it is likely that the two enhancements at $t = 1742.15$ and $t = 1742.20$ are the decay phases of the same flare. It is also possible that the three enhancements observed at $t = 1742.15$, 1742.20 , and 1742.28 days are parts of a complex flare with two peaks. The total exposure time during the three enhancements is 2820 s, and the total time including the gaps between the flares is 12,700 s (3.5 hr). Furthermore, the upper limit in total duration of this complex flare is 12.1 hr. The X-ray energy emitted during the exposure time is $\log E$ (erg) = 32.6. No optical flares were observed by TESS during these times.

4.5. LCOGT Light Curve

The EV Lac light curve obtained by LCOGT is shown in Figure 11. The subplot on the left shows the light curve that was obtained on 2019 September 17, and the subplot on the right shows the one obtained on 2019 September 21. As seen in the figure, one full flare was observed by LCOGT at $t = 1749.89$ days, and the observed peak flux was $\sim 20\%$ brighter than quiescence. Only NICER observed the star simultaneously during the time of this flare. However, we do not notice a clear flare-like event in the NICER light curve during that time. There is a very slight enhancement in X-ray level with respect to the median value (M_N), but is within the $M_N + 2.5\sigma_N$ value. Thus, it is hard to decide if it is due to flare or other factors such as instrumental effects. Fluctuations in the quiescent level can be seen in the light curve during other times as well. The LCOGT flare occurred during the TESS data downlink time. As a result, we have no information from TESS about this event. We might have observed the decay phase of a flare in the light curve shown in the left subplot. However, we do not see a flare during the same time in TESS light curve.

We estimate the U -band flare energy using a method analogous to that for the UVOT flares. We compute the equivalent duration (827 s) of the flare by first normalizing the light curve with a linear fit (masking the time span of the flare), integrating over the 13 minute period (792 s) that includes the flare rise time and the decay (until it becomes indistinguishable from the quiescent flux level). A U -band magnitude measurement is unavailable for EV Lac in the literature, so we estimate it based off the B -band magnitude (11.85 mag; Zacharias et al. 2012) and the $U-B = 1.22$ color for M4 dwarfs from Pecaut & Mamajek (2013). Using the published zero-point magnitude flux for the U band and mean width of the filter (Bessell et al. 1998) and distance to EV Lac, we estimate EV Lac’s quiescent luminosity in the U band to be 4.6×10^{28} erg s $^{-1}$. With the equivalent duration measured from the light curve, we find the U -band energy of the flare to be 3.8×10^{31} erg.

4.6. Flare Observed Simultaneously by TESS, Swift/UVOT, and NICER

The flare T6 observed by TESS at $t = 1749.29$ days was partly observed simultaneously by Swift/UVOT (ID: U7) as well as by NICER (ID: N9). The total duration of this flare in the TESS band is 25.9 minutes. Swift/UVOT observed only the rise phase and the initial decay phase of the flare for 1.3 minutes. NICER observed only a part of the decay phase during which X-ray flux was almost constant for 12.6 minutes. This flare is shown in Figure 12. In the TESS band, the energy of this flare is estimated to be equal to $\log E_T$ (erg) = 31.8, and in UVM2 band, the energy is estimated to be $\log E_U$ (erg) > 31.1. Likewise, the estimated energy of this flare in NICER band is $\log E_N$ (erg) > 31.7.

Table 3
Properties of Flares Observed by TESS

Flare ID	Peak Time (T_0) BJD—2457000	FWHM min	Amplitude relative flux	ED seconds	$\log E_T$ erg
1	1738.82433714	64	0.027674	14.1	32.06
2 (T1)	1739.21878855	202	0.122476	72.4	32.77
3 (T2)	1740.22574895	40	0.009205	16.5	32.13
4	1740.36880662	162	0.174420	53.9	32.64
5	1740.41186281	18	0.023720	164.6	33.13
6	1740.87020271	114	0.057260	188.7	33.19
7	1741.02992716	148	0.024194	25.3	32.31
8 (T3)	1741.3021531	20	0.014463	6.2	31.70
9	1741.57437895	102	0.011378	5.9	31.68
10	1742.24938761	186	0.006970	31.7	32.41
11	1742.62717002	30	0.005604	11.8	31.98
12	1742.82856132	74	0.007248	15.9	32.11
13 (T4)	1742.93272922	50	0.014444	5.4	31.65
14	1743.27439985	4	0.004253	3.5	31.46
15	1743.2882889	34	0.016011	9.2	31.88
16	1743.93690724	24	0.008897	4.2	31.53
17	1744.1410761	44	0.004129	10.8	31.94
18	1745.58970178	10	0.001775	1.0	30.92
19	1745.6049797	26	0.001949	2.7	31.34
20	1746.13692908	24	0.002729	5.8	31.68
21 (T5)	1746.50498793	34	0.024221	9.6	31.89
22	1746.93693614	96	0.007408	8.5	31.84
23	1747.50916321	76	0.021192	8.1	31.82
24	1748.52306041	22	0.007969	4.3	31.54
25	1748.61195002	68	0.011904	7.0	31.76
26	1749.06473153	60	0.012007	4.3	31.55
27 (T6)	1749.29667793	122	0.013921	7.7	31.80
28 (T7)	1749.58279152	236	0.292071	158.0	33.11
29	1749.59945834	4	0.017898	3.7	31.48
30	1749.60501394	4	0.015053	41.0	32.52
31	1749.81334917	120	0.010527	39.8	32.51
32	1750.14529684	6	0.002878	0.9	30.85
33	1751.91198033	318	0.007173	14.7	32.08
34	1752.72309347	58	0.006594	13.2	32.03
35	1752.8661492	120	0.006238	29.8	32.39
36	1753.31614945	94	0.033520	27.0	32.34
37	1753.58003832	54	0.006111	6.2	31.71
38	1753.66892718	6	0.009420	3.4	31.44
39	1753.67726051	16	0.002388	2.1	31.23
40	1754.28281555	4	0.001950	0.5	30.57
41	1754.41614871	104	0.006912	10.2	31.92
42	1754.7994814	182	0.008560	16.3	32.12
43	1755.50225756	4	0.002204	0.4	30.51
44	1755.87308981	40	0.003324	9.0	31.87
45	1756.48142107	24	0.003474	7.0	31.76
46 (T8)	1757.80085975	38	0.006203	9.1	31.87
47	1757.8966926	128	0.039899	84.2	32.84
48	1758.12863584	118	0.014824	72.5	32.77
49 (T9)	1759.47168357	228	0.056124	37.3	32.48
50	1760.13140146	22	0.004910	6.4	31.72
51	1760.21612311	56	0.009914	9.9	31.91
52	1760.27584492	158	0.008755	36.7	32.48
53	1760.70084196	184	0.012990	59.3	32.68
54	1762.44110719	108	0.032657	13.2	32.03
55	1762.63416142	128	0.048114	28.9	32.37
56	1762.99110355	80	0.004179	20.6	32.23

4.7. Flare Observed Simultaneously by Swift/UVOT and NICER

In addition to U7/N9, another flare, U8/N11, shown in Figure 13, was observed simultaneously by Swift/UVOT and NICER. However, neither mission observed the flare for its full

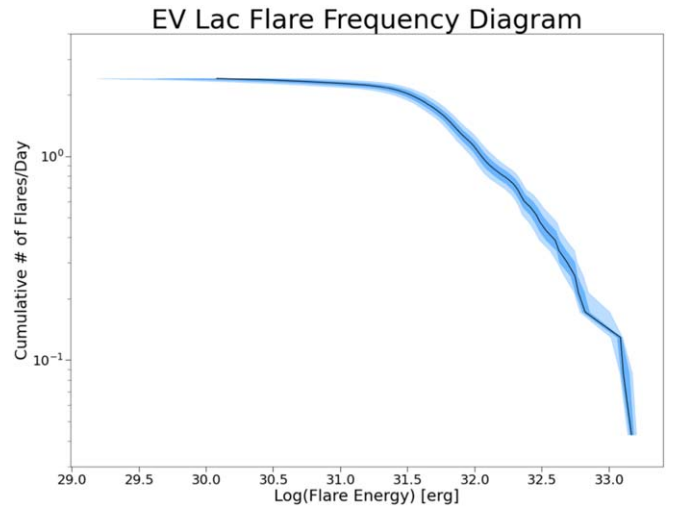


Figure 5. Flare frequency distribution (FFD) of EV Lac and its associated 1σ uncertainty (shading) determined from our modeling of the TESS data. The TESS white light flares follow the expected power-law distribution from $10^{31.5}$ – 10^{33} erg. It is harder to detect lower-energy flares due to their small amplitudes and durations, resulting in the flattening of the FFD at low energies. Larger flares that occur less frequently may not be seen in the observing baseline of a single TESS sector.

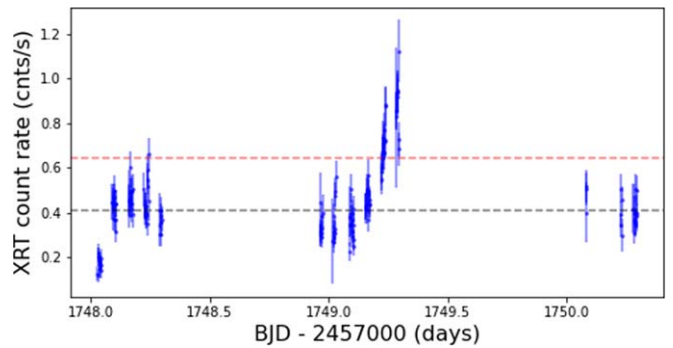


Figure 6. Swift XRT light curve of EV Lac with 120 s time bins. The black and red dashed lines correspond to median and median+ 1σ count rates. We cannot confirm that the increase in X-rays at $t \sim 1749.3$ days is due to a flare.

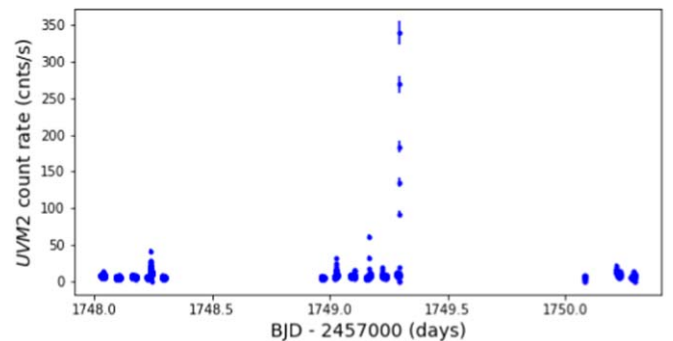


Figure 7. Swift UVOT light curve of EV Lac. The time binning is 11.033 s. We identified nine flares in this light curve.

duration. NICER observed it during the rise phase for 8.2 minutes, and UVOT observed it during the decay phase for 11.2 minutes. The estimated energy of this flare is $\log E_N$ (erg) > 31.3 in the NICER band and $\log E_U$ (erg) > 30.5 in the UVM2 band. This flare occurred during the TESS data downlink period, so we do not have its TESS light curve.

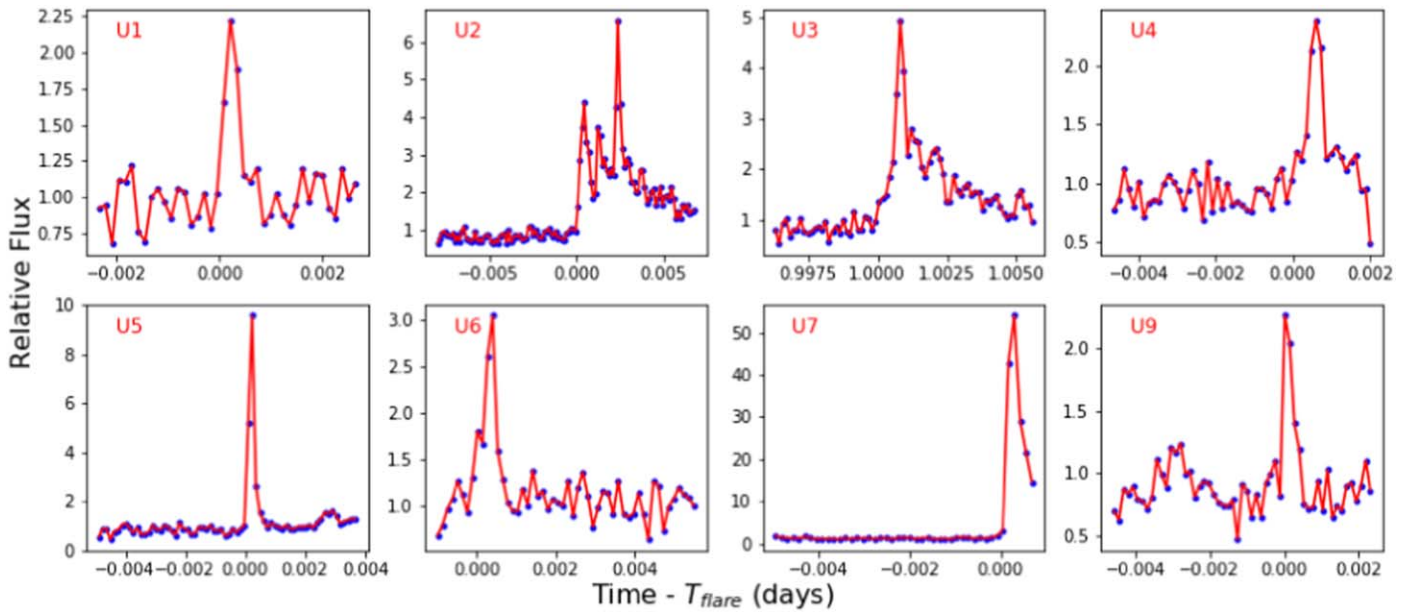


Figure 8. Individual flares observed by Swift UVOT. The blue dots in each plot represent the observed fluxes, and the red line is the connecting line. The time axis is centered at T_0 , which is the TESS time when a given flare started. The time binning is 11.033 s. One of the UVOT flares, U8, was only observed during the decay phase and is not shown here.

Table 4
Properties of Flares Observed by Swift UVOT

Flare ID	Time start (T_0) BJD— 2457000	Time stop BJD— 2457000	Duration min	ED min	Energy 10^{30} erg
U1	1748.0401	1748.0408	0.92	0.77	0.40
U2	1748.2379		>9.6	>16.3	>8.4
U3	1749.0260	1749.0314	7.7	6.7	3.4
U4	1749.1059	1749.1075	2.2	1.1	0.57
U5	1749.1663	1749.1669	0.74	2.8	1.4
U6	1749.2232	1749.2238	0.92	0.93	0.48
U7	1749.2952		>1.3	>26.0	>13.3
U8		1750.2256	>11.2	>6.7	>3.4
U9	1750.2913	1750.2917	0.55	0.43	0.22

The flares U1, U2, U3, U4, U5, U6, and U9 were observed during data gaps in the NICER light curve. Likewise, no flares were observed simultaneously by TESS and Swift UVOT except the flare T6. There is a weak indication of flux enhancement in the TESS light curve during U2, but it is within the noise level of the light curve and hence is not detected by bayesflare.

4.8. Flares Observed Simultaneously by TESS and NICER

Nine flares were observed simultaneously by TESS and NICER. Eight of them are shown in Figure 14. The remaining flare is N1, which was observed during its initial rise phase simultaneously for 219 s with NICER. The flare ID and the mission name are mentioned inside each subplot. The red dashed line in the subplots showing NICER flares corresponds to the quiescent level (M_N) in the NICER light curve.

In Table 7, we compare the TESS flare energies E_T as well as corresponding bolometric flare energies E_{bol} with the NICER flare energies for the above nine flares. Because of the incomplete information about the flares in NICER data, we

can only estimate an upper limit on the ratios E_T/E_N and E_{bol}/E_N . An estimation of X-ray flare energies by considering the duration of corresponding flares observed in TESS data is listed in Table 6 in column “log E_T ”.

4.9. Comparison of Quiescent Luminosity in Various Bands to Bolometric Luminosity

In Table 8, we list the values of quiescent fluxes of EV Lac which we estimated for various bands in which the star was observed. In addition, we compare those fluxes with the flux in the TESS band. Such ratios will be helpful to estimate the total energy output of a TESS target with comparable spectral type and age as EV Lac.

4.10. Analysis of the FIP/IFIP Effect

In the case of active regions in the solar corona, the elements with low First Ionization Potential (FIP) are found to be more abundant than those with high FIP (above ~ 10 eV) when compared to their photospheric abundances. This is known as the FIP effect (Feldman 1992). While certain stars also show evidence of a solar-like FIP effect, some active stars also show an Inverse FIP (IFIP) effect where the high-FIP elements are more abundant compared to the low-FIP elements in the corona relative to their photospheric abundances (Brinkman et al. 2001). Studies of flares on different stars show mixed results regarding how the flares affect the FIP pattern. Güdel et al. (1999), Audard et al. (2001), and Raassen et al. (2003) reported an increase in low-FIP abundances during flares on UX Ari, HR 1099, and AT Mic, respectively. However, Osten et al. (2003), Güdel et al. (2004), and Raassen et al. (2007) did not observe such an effect during flares from other targets, namely σ^2 Coronae Borealis, Proxima Centauri, and YZ CMi.

We list the abundances of five elements: oxygen (O), neon (Ne), magnesium (Mg), silicon (Si), and sulfur (S) in Table 9 obtained by fitting the spectrum (using `xspec`) of the quiescent level of the star, and those of the eight largest flares:

Table 5
NICER Flares Spectral Fit Results

flare ID	N0	N1	N2	N3	N4(peak)	N5	N6	N7	N8
X-ray band (keV)	0.3–3.0	0.3–2.0	0.3–3.0	0.3–3.0	0.3–3.0	0.3–3.0	0.3–2.0	0.3–3.0	0.3–3.0
T_1 (MK)	$3.0^{+0.5}_{-0.4}$	$2.8^{+0.5}_{-0.4}$	$3.5^{+2.0}_{-1.5}$	$3.1^{+0.2}_{-0.1}$	$4.8^{+1.3}_{-1.7}$	$5.7^{+0.9}_{-1.0}$	$5.2^{+1.4}_{-0.7}$	$2.9^{+0.2}_{-0.2}$	$3.5^{+1.8}_{-0.7}$
EM_1 (10^{51} cm $^{-3}$)	$1.2^{+0.3}_{-0.3}$	$1.2^{+0.3}_{-0.3}$	$1.2^{+0.6}_{-0.6}$	$1.2^{+0.3}_{-0.3}$	$1.8^{+1.2}_{-1.2}$	$3.7^{+0.9}_{-0.9}$	$3.1^{+1.2}_{-1.2}$	$1.2^{+0.3}_{-0.3}$	$1.1^{+0.3}_{-0.6}$
T_2 (MK)	$9.2^{+0.4}_{-0.5}$	$7.5^{+1.9}_{-1.4}$	$9.3^{+1.6}_{-0.6}$	$7.9^{+0.6}_{-0.5}$	$9.4^{+2.1}_{-1.3}$	$11.6^{+0.7}_{-0.8}$	$11.4^{+0.8}_{-0.9}$	$8.7^{+0.5}_{-0.7}$	$8.5^{+0.6}_{-0.8}$
EM_2 (10^{51} cm $^{-3}$)	$3.7^{+0.9}_{-0.9}$	$1.1^{+0.6}_{-0.3}$	$6.1^{+2.7}_{-1.3}$	$2.9^{+0.9}_{-0.6}$	$3.7^{+1.2}_{-0.9}$	$7.6^{+1.8}_{-1.8}$	$6.4^{+1.8}_{-1.5}$	$2.4^{+0.9}_{-0.6}$	$3.4^{+1.2}_{-0.9}$
T_3 (MK)	$24.4^{+2.6}_{-1.5}$	$24.4^{+12.8}_{-5.8}$	$25.5^{+13.1}_{-3.6}$	$22.0^{+2.4}_{-2.2}$	$23.2^{+1.3}_{-1.3}$	$29.0^{+4.2}_{-2.9}$...	$24.4^{+3.0}_{-2.1}$	$22.0^{+2.3}_{-2.2}$
EM_3 (10^{51} cm $^{-3}$)	$11.0^{+0.6}_{-0.6}$	$2.3^{+0.3}_{-0.6}$	$4.3^{+0.9}_{-1.2}$	$2.8^{+0.3}_{-0.3}$	$9.0^{+0.6}_{-1.8}$	$15.6^{+1.5}_{-1.8}$...	$4.3^{+0.3}_{-0.3}$	$4.3^{+0.3}_{-0.6}$
reduced χ^2 , dof	1.1, 206	1.2, 97	0.97, 164	1.1, 176	1.1, 214	1.0, 242	0.95, 113	1.0, 169	1.0, 180
F-test prob.	2.6e-06	2.1e-06	0.02	4.2e-08	2.2e-04	4.6e-08	0.95	2.9e-09	4.9e-4
flare ID	N9	N10	N11	N12	N13	Quies.			
X-ray band (keV)	0.3–3.0	0.3–3.0	0.3–3.0	0.3–3.0	0.3–3.0	0.3–2.0			
T_1 (MK)	$3.0^{+0.4}_{-0.2}$	$4.9^{+0.7}_{-0.5}$	$3.0^{+0.4}_{-0.4}$	$3.0^{+0.1}_{-0.2}$	$3.1^{+0.7}_{-0.4}$	$2.9^{+0.1}_{-0.1}$			
EM_1 (10^{51} cm $^{-3}$)	$1.6^{+0.3}_{-0.3}$	$3.4^{+0.6}_{-0.6}$	$0.8^{+0.3}_{-0.3}$	$1.1^{+0.3}_{-0.3}$	$1.5^{+0.6}_{-0.6}$	$1.0^{+0.1}_{-0.1}$			
T_2 (MK)	$7.7^{+0.8}_{-0.6}$	$11.5^{+0.7}_{-0.8}$	$8.8^{+0.7}_{-0.9}$	$9.2^{+0.4}_{-0.5}$	$7.5^{+1.3}_{-1.6}$	$7.8^{+0.1}_{-0.1}$			
EM_2 (10^{51} cm $^{-3}$)	$2.9^{+0.9}_{-0.6}$	$7.3^{+2.1}_{-1.8}$	$1.7^{+0.9}_{-0.6}$	$2.8^{+0.6}_{-0.6}$	$1.5^{+0.9}_{-0.6}$	$1.9^{+0.2}_{-0.2}$			
T_3 (MK)	$24.4^{+2.0}_{-1.7}$	$23.2^{+4.8}_{-2.4}$	$29.0^{+5.3}_{-4.2}$	$29.0^{+3.2}_{-2.9}$	$27.8^{+4.6}_{-3.8}$	$20.9^{+2.3}_{-1.6}$			
EM_3 (10^{51} cm $^{-3}$)	$5.8^{+0.3}_{-0.3}$	$8.9^{+1.5}_{-1.8}$	$3.7^{+0.3}_{-0.3}$	$4.8^{+0.3}_{-0.3}$	$7.3^{+0.6}_{-0.6}$	$0.70^{+0.1}_{-0.1}$			
reduced χ^2 , dof	1.1, 190	1.1, 213	0.83, 157	1.0, 208	1.0, 137	1.2, 157			
F-test prob.	3.1e-27	1.5e-08	1.2e-06	6.4e-12	4.0e-4	7.6e-16			

N0, N2, N4, N5, N8, N9, N10, and N13. All the abundances are expressed relative to iron (Fe). We were not able to fit the abundance of S in the quiescent level properly, therefore a default value of 1.0 is listed in the table. For each flare, we compare the abundances of four elements, O, Ne, Mg, and Si, with respect to the quiescent level. Such values are listed in the columns “Flare/Quies.” Using these ratios, we analyze the FIP/IFIP effect during the eight largest flares on EV Lac.

In Figure 15, we plot the values of abundance ratios “Flare/Quies.” of four elements: O (black triangle), Ne (blue square), Mg (red circle), and Si (pink diamond) as a function of the FIP of elements. The values of FIP of O, Ne, Mg, and Si are 13.62, 21.56, 7.65, and 8.15 eV, respectively. So among these four elements, O and Ne are high-FIP elements and the other two are low-FIP elements. The dashed horizontal line in each subplot corresponds to the abundance ratio of the elements during quiescent state of the star. The flare label is mentioned inside each subplot. The plots suggest that low-FIP element Mg showed no significant change in abundance during seven flares except during flare N5. The large ratio for Mg during flare N2 is due to the fact that its real value could not be fitted and a default value equal to 1.0 was used during spectral fitting. Another low-FIP element Si also showed no significant change during four flares and is found to be underabundant during the remaining four flares. While O is found to be underabundant compared to the quiescent value during one flare and overabundant during one flare, Ne is found to be underabundant compared to the quiescent value during three flares. In general, we cannot identify with confidence any overall patterns regarding the FIP effect in the EV Lac flares we have reported here.

5. Summary and Discussion

We acquired data of the nearby dM3.5e star EV Lac using five different observatories: NASA’s TESS mission, NASA’s Neil Gehrels Swift Observatory (Swift), NASA’s Neutron Interior Composition Explorer (NICER), and two ground-based

telescopes (University of Hawaii 2.2-meter (UH88) and Las Cumbres Observatory Global Telescope (LCOGT) Network). Our goal was to carefully characterize an ensemble of flaring events observed simultaneously in different wavelengths to understand how flare energies and frequencies are related at different wavelengths. During the ~ 24 days of continuous TESS Cycle 2 observations, we acquired three simultaneous 18 ks UV/X-ray observations using Swift, 21 simultaneous 97.7 ks X-ray observations using NICER, ~ 3.0 hr of ground-based observation with UH88, and ~ 3.0 hr of ground-based observation with LCOGT.

We identified 56 white light flares in the TESS light curve, with estimated energies in the range $\log E_T$ (erg) = (30.5–33.2). Nine UV flares were identified in the Swift/UVOT light curve, with estimated energies in the range $\log E_{UV}$ (erg) = (29.3–31.1), but three were not observed throughout their full duration. Likewise, we identified 14 X-ray flares in the NICER light curve, with estimated minimum energies in the range $\log E_N$ (erg) = (30.5–32.3). One flare with an estimated energy $\log E_L$ (erg) = 31.6 was identified in the LCOGT light curve. One flare was observed simultaneously by TESS, UVOT, and NICER during various phases. While UVOT observed the rise and initial decay phase, NICER observed the later part of the decay phase. NICER and UVOT observed different phases of another flare. Likewise, TESS and NICER observed nine flares simultaneously. We did not identify any flares in the Swift/XRT or UH88 light curves.

In general, we might expect to observe flares in X-rays and UV simultaneously, but this was not the case during the observation by Swift. However, it is also possible to see UV flares without X-ray flares, because the two flare signatures are formed in different parts of the stellar atmosphere: the lack of correspondence implies that energy release is happening so low in the atmosphere that the chromospheric response (detected by Swift/UVOT) is dominant. The lack of an X-ray flare implies that the corona is not involved in the event, perhaps because of a deficiency in the amount of evaporated chromospheric material. In contrast, in the standard scenario of a flare, the

Table 6
Properties of Flares Observed by NICER

Flare ID	Flare time BJD—2457000	Phase	X-ray band keV	Duration			Av. flux 10^{-11} $\text{erg cm}^{-2} \text{s}^{-1}$	F_f/F_q	Energy		
				t_N sec	t_T sec	$t_{N,\text{gaps}}$ hr			$\log E_{\text{min},N}$ erg	$\log E_T$ erg	$\log E_{N,\text{gaps}}$ erg
N0	1739.25	decay	0.3–3.0	574	5400	10.6	5.1	3.9	32.0	33.0	33.8
N1	1740.22	rise	0.3–2.0	219	1814	1.5	0.5	0.4	30.5	31.4	31.9
N2	1741.11	...	0.3–3.0	470		21.3	2.6	2.0	31.6		33.8
N3	1741.31	decay	0.3–3.0	952	950	1.5	1.5	1.2	31.6	31.6	32.4
N4	1742.15	peak/decay	0.3–3.0	1864		3.1	2.5	1.9	32.1		32.9
N5	1742.28	decay	0.3–3.0	956		9.0	7.5	5.8	32.3		33.9
N6	1742.86	...	0.3–2.0	239		4.4	1.7	1.3	31.1		32.9
N7	1742.92	rise	0.3–3.0	910	1080	1.6	1.9	1.5	31.7	31.8	32.5
N8	1746.6	peak/decay	0.3–3.0	731	1443	1.6	2.1	1.6	31.7	32.4	32.6
N9	1749.31	...	0.3–3.0	756	1555	7.5	2.4	1.9	31.7	32.1	33.3
N10	1749.63	decay	0.3–3.0	839	11163	7.5	5.5	4.2	32.2	33.3	33.7
N11	1750.21	rise	0.3–3.0	489		3.0	1.3	1.0	31.3		32.6
N12	1757.82	peak/decay	0.3–3.0	1088	1322	19.8	2.3	1.8	31.9	32.0	33.7
N13	1759.51	...	0.3–3.0	230	6005	1.4	2.7	2.1	31.3	32.7	32.6

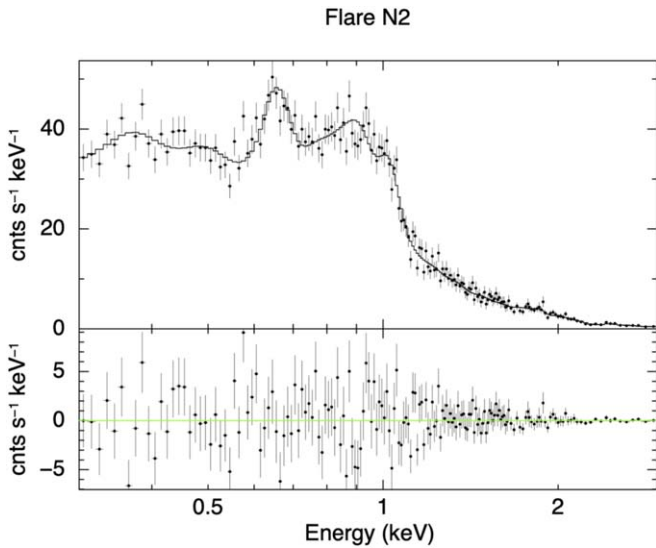


Figure 9. An example of fitting of an X-ray flare spectrum by using `xspec`. The upper panel shows the data and 3T VAPEC model (solid line), and the lower panel shows the residuals. The complete figure set (15 images) is available in the online journal.

(The complete figure set (15 images) is available.)

energy input from magnetic reconnection and accelerated particles heats chromospheric material on a timescale that is short compared with the hydrodynamic expansion time, causing the ablation of chromospheric material (now heated to coronal temperatures) up the loop legs, which produces X-ray radiation.

In order to ascertain the physical properties of the X-ray flares, we fitted the NICER flare spectra using a three-discrete-temperature (3T) plasma model in Section 4.4. The temperatures (T_1) of the coolest component range from 2.8 to 5.7 MK. We interpret the quiescent (i.e., non-flaring) corona as the origin of the T_1 component. Flares are expected to be confined to a relatively small area on the stellar surface, of order 1% for white light flares and perhaps as large as 10% for the Balmer line-emitting region (see Cram & Woods 1982). EV Lac’s quiet corona likely has temperatures of a few million degrees and might occupy 90% or more of the surface area during the time

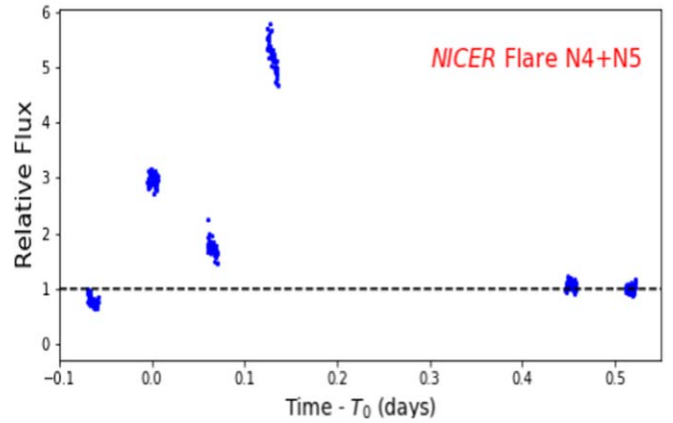


Figure 10. Flares observed by NICER in between $t = 1742.10$ and $t = 1742.60$ days. The black dashed line corresponds to the quiescent level (M_N). The time along the X-axis is centered at $T_0 = 1742.15$ days.

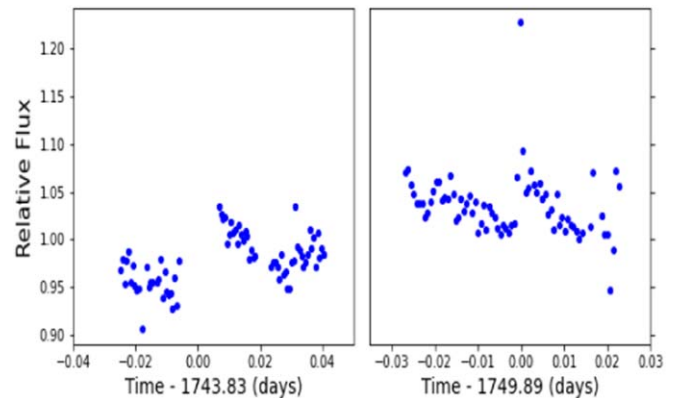


Figure 11. Light curve of EV Lac obtained by LCOGT, on 2019 September 17, (left) and on 2019 September 21. A large flare was observed at $t = 1749.89$ days.

of the flare. In partial support of this claim, we note that Osten et al. (2006) estimated the differential emission measure (DEM) for the quiescent atmosphere of EV Lac and they found that it peaks at $T = 2.5$ MK, which overlaps within the error bars of the values of T_1 listed in Table 5 above. The temperatures (T_2) of the second component have values ranging from 7.5 to

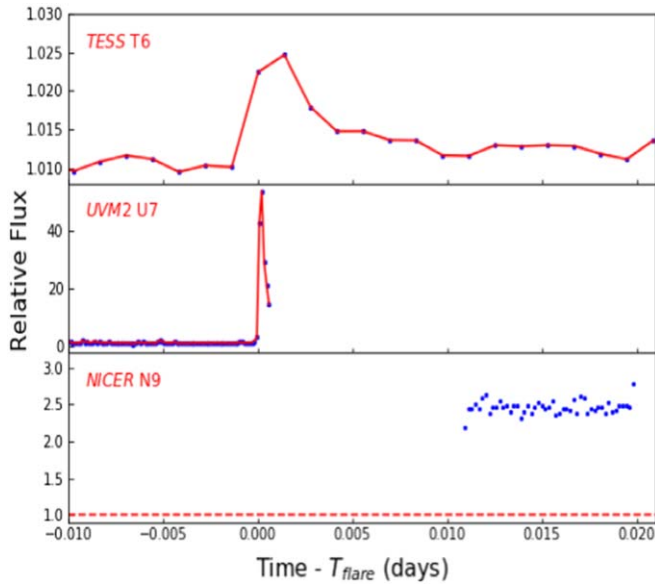


Figure 12. Flare observed simultaneously by TESS, Swift/UVOT, and NICER. Note that the cadence length of TESS data is 2.0 minutes, Swift/UVOT is 11.033 s, and that of NICER data is 5.0 s. The red dashed line in the lowermost subplot corresponds to the quiescent level (M_N) in the NICER light curve.

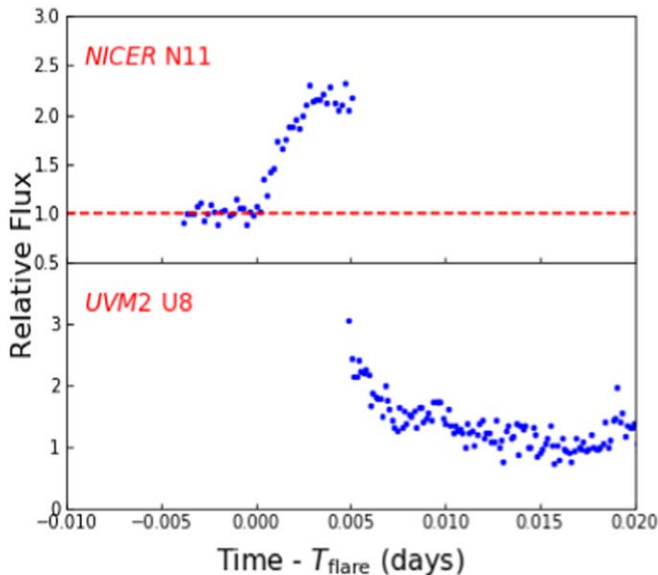


Figure 13. Flare observed simultaneously by NICER and Swift UVOT. The cadence length of UVOT data is 11.033 s, and that of NICER is 5.0 s. The red dashed lines in the subplot showing NICER flares correspond to the quiescent level (M_N) in the NICER light curve.

11.5 MK. We interpret these temperatures as being due to a hotter component of the quiescent corona in EV Lac. Osten et al. (2006) also found a secondary peak in the DEM for a quiescent EV Lac at $T = 7.9$ MK, which overlaps with the range of values we have obtained from NICER data for the quantity T_2 . We find the temperatures T_3 of the third component have values from 22.0–29.0 MK and correspond to the flaring corona. Osten et al. (2005) analyzed nine X-ray flares observed by Chandra with a $2T$ plasma model and found that, for all but two flares, the hotter (i.e. flaring) component had values in a range similar to our T_3 components, lending confidence to our interpretation.

Taking into account the minimum X-ray flare energies observed by NICER, we estimated the maximum energy ratio of optical and X-ray flares observed by TESS and NICER. We find that the ratio exceeds unity for almost all flares, and does so by an order of magnitude for the larger flares. These results are to some extent consistent with the results of Schmitt et al. (2019), who analyzed a sample of eight superflares (with energies $\geq 10^{34}$ erg) on another flare star (AB Doradus), which were detected by TESS in the course of about two months of observations. The TESS energies ranged from $1\text{--}50 \times 10^{34}$ erg. They also compared the energies of those flares to those of 34 X-ray flares (with energies in the range $\log E = 30.03$ to 33.83) observed on the same star by XMM-Newton in a period of 11 yr (Lalitha 2016) and to that of the largest solar flare seen in solar irradiance measurements. They found, on average, the total X-ray energy of flares on AB Dor to be less than the energy in optical (super)flares. In an earlier paper, Mullan (1976a) used the values of time scales of radiative energy loss and conductive energy loss to estimate the ratio of luminosities in X-rays and in optical photons: L_X/L_{opt} . He found that L_X/L_{opt} would be no larger than 0.1 (sometimes considerably less than 0.1). The conclusions of Schmitt et al. (2019) and Mullan (1976a) suggest that the ratios of flare energies we have estimated in Table 7 may not be significantly different from the real values.

We searched for the FIP/IFIP effect using the abundances of four elements (O, Ne, Mg, and Si) during the eight largest NICER flares. We find that two elements, Ne (high-FIP element) and Si (low-FIP element), both are underabundant relative to the quiescent state during three flares, and Si is underabundant in one more flare. In an exceptional flare, Ne was found to be underabundant relative to the quiescent state. The next-highest-FIP element studied, O, was found to be underabundant in one of the NICER flares and overabundant in another flare. The low-FIP element Mg was neither overabundant nor underabundant relative to the quiescent state in all flares except one. Thus, we cannot draw any definite conclusions regarding a pattern of either FIP or IFIP during the EV Lac NICER flares.

Oscillatory and pulsating signatures known as quasi-periodic pulsations (QPPs) are a common feature observed in the light curves of both solar and stellar flares (see, e.g., Vida et al. 2019 (TESS), Pugh et al. 2016 (Kepler), Jackman et al. 2019 (NGTS), Broomhall et al. 2019 (XMM-Newton), and Inglis et al. 2016 (in solar flares)). These oscillations can provide constraints on the mechanisms of flare production and the properties of the stellar atmosphere. This includes: thermal free-free microwave emission of chromospheric plasma heated during a flare and filling in the flaring loop (Kupriyanova et al. 2014), modulation of the nonthermal electron dynamics by MHD oscillations (Zaitsev & Stepanov 1982), and the triggering of energy released by external MHD waves or oscillations (Chen & Priest 2006; Nakariakov et al. 2006, 2016). QPP periods can range from a fraction of a second to several minutes (Nakariakov et al. 2016; Van Doorselaere et al. 2016). The short-lived nature and short periods of QPPs make the Swift/UVOT and NICER data presented here, with cadences of ~ 10 s, ideal for a follow-up study to search for and analyze QPPs in stellar flare morphology. We will present our results regarding QPPs in EV Lac flares in Monsue T. et al. (2021, in preparation).

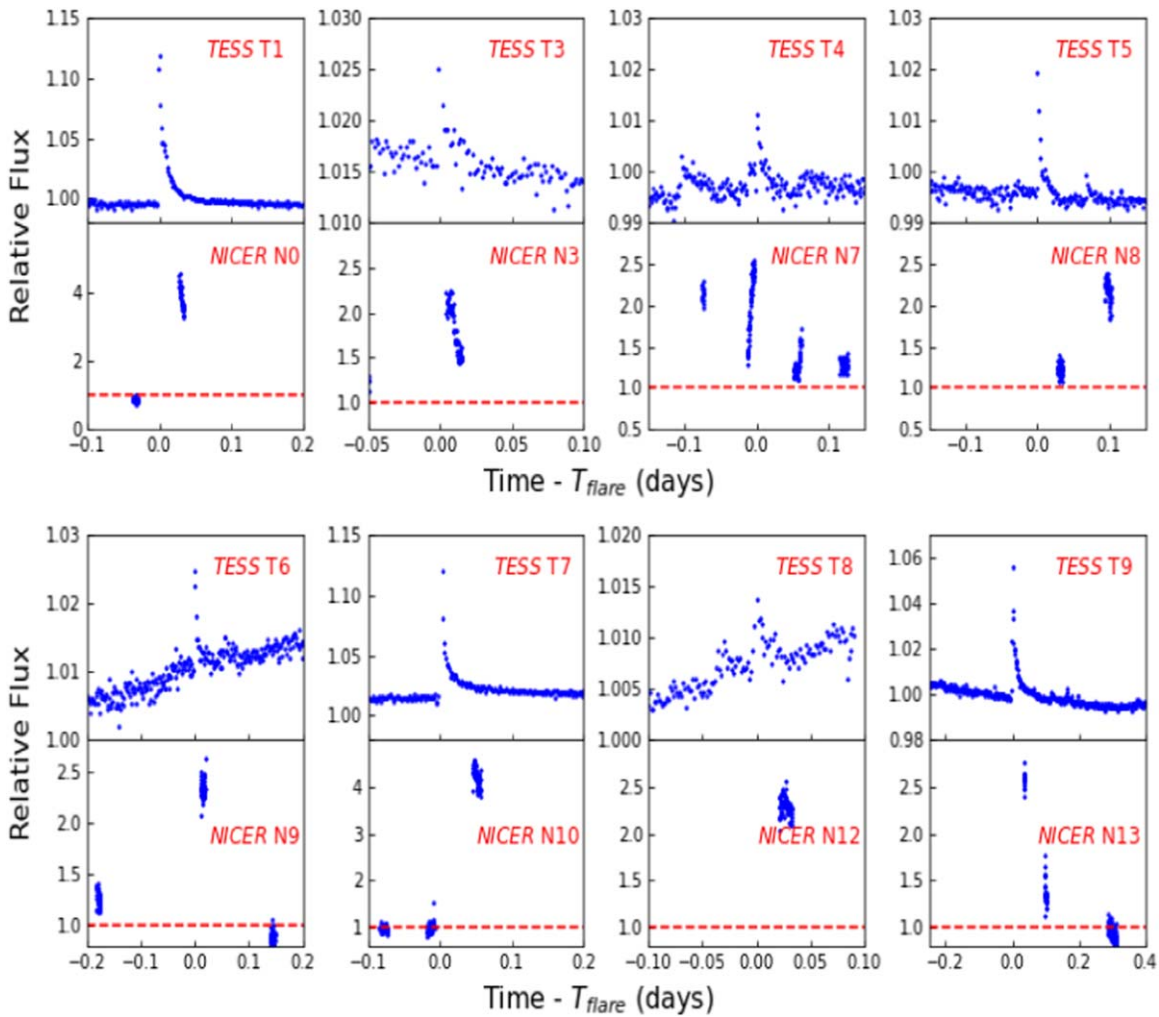


Figure 14. Flares observed simultaneously by TESS and NICER. The red dashed line in the subplots showing NICER flares correspond to the quiescent level (M_N) in the NICER light curve. The cadence length of TESS data is 2.0 minutes, and that of NICER is 5.0 s.

Table 7
Comparison of Flare Energies E_T and E_N

Flare ID	$\log E_T$ erg	$\log E_{\text{bol}}$ erg	$\log E_N$ erg	$(E_T/E_N)_{\text{max}}$
T1/N0	32.8	33.6	32.0	6.3
T2/N1	32.1	32.9	30.5	40.0
T3/N3	31.7	32.5	31.6	1.3
T4/N7	31.7	32.5	31.7	1.0
T5/N8	31.9	32.7	31.7	1.6
T6/N9	31.8	32.6	31.7	1.3
T7/N10	33.1	33.9	32.2	8.0
T8/N12	31.9	32.7	31.9	1.0
T9/N13	32.5	33.3	31.3	15.8

Table 8
Quiescent Luminosity in Various Bands

Band	$\log L_Q$ erg s^{-1}	$\log L_Q/L_{\text{bol}}$
TESS	30.9	-0.79
Swift XRT	28.5 (0.3–2.0 keV)	-3.2
Swift UVM2	27.9	-3.8
NICER	28.6 (0.3–2.0 keV)	-3.1
LCO	28.7	-3.0

5.1. Comparison of Flare Frequency Distributions

For each of the three spectral bands in which we have observed multiple flares (TESS, Swift/UVOT, and NICER), we have used least-squares fitting to obtain an FFD described by power-law index β (Table 10). We used Poisson uncertainties to weight the fit, which helps to minimize the bias due to potential overweighting of the largest flare energies. We also list the values of the minimum and maximum energies, as well as the number of flares used for fitting. The errors are obtained by dividing the values of β by \sqrt{N} , where N is the number of flares used for fitting.

In Figure 16, we compare the FFDs of flares observed by TESS, NICER, and Swift/UVOT. The X-ray FFD in this figure is estimated by using the same observation time (i.e., 23.2 days) as TESS.²⁹ We remind the readers that the FFD of NICER data is estimated by using the lower limit of all flare energies, as none of the flares were observed for the full duration. It is interesting to note that the slopes of the FFDs corresponding to TESS and NICER data are comparable. This might be due to the fact that the flares observed on EV Lac by

²⁹ Since NICER observations were performed throughout a single TESS sector (~ 25 days), using the total exposure time (~ 98 ks) of NICER to estimate the FFD would result in flare rates higher than the real values.

Table 9
Abundances Measured Relative to Fe During a Flare Compared to the Quiescent State

El	Quies. X/Fe	Flare N0		Flare N2		Flare N4		Flare N5	
		X/Fe	Flare/Quies.	X/Fe	Flare/Quies.	X/Fe	Flare/Quies.	X/Fe	Flare/Quies.
O	$0.56^{+0.02}_{-0.02}$	$0.73^{+0.11}_{-0.09}$	$1.30^{+0.20}_{-0.17}$	$0.60^{+0.11}_{-0.08}$	$1.07^{+0.20}_{-0.15}$	$0.45^{+0.06}_{-0.05}$	$0.80^{+0.11}_{-0.11}$	$0.52^{+0.06}_{-0.05}$	$0.93^{+0.11}_{-0.10}$
Ne	$1.42^{+0.10}_{-0.10}$	$1.73^{+0.61}_{-0.51}$	$1.22^{+0.44}_{-0.37}$	$0.9^{+0.43}_{-0.34}$	$0.63^{+0.31}_{-0.24}$	$0.90^{+0.55}_{-0.41}$	$0.63^{+0.39}_{-0.29}$	$0.55^{+0.23}_{-0.21}$	$0.38^{+0.16}_{-0.15}$
Mg	$0.42^{+0.06}_{-0.05}$	$0.56^{+0.26}_{-0.22}$	$1.33^{+0.65}_{-0.55}$	1.0		$0.32^{+0.15}_{-0.16}$	$0.76^{+0.37}_{-0.39}$	$0.23^{+0.12}_{-0.11}$	$0.55^{+0.30}_{-0.27}$
Si	$0.63^{+0.07}_{-0.06}$	$0.63^{+0.18}_{-0.16}$	$1.0^{+0.31}_{-0.27}$	$0.24^{+0.14}_{-0.13}$	$0.39^{+0.23}_{-0.21}$	$0.42^{+0.11}_{-0.11}$	$0.67^{+0.19}_{-0.19}$	$0.30^{+0.08}_{-0.08}$	$0.48^{+0.14}_{-0.13}$
S	$0.41^{+0.10}_{-0.10}$	$0.65^{+0.25}_{-0.25}$		$0.38^{+0.29}_{-0.29}$		$0.38^{+0.17}_{-0.17}$		$0.50^{+0.14}_{-0.14}$	
		Flare N8		Flare N9		Flare N10		Flare N13	
	X/Fe	X/Fe	Flare/Quies.	X/Fe	Flare/Quies.	X/Fe	Flare/Quies.	X/Fe	Flare/Quies.
O	$0.56^{+0.02}_{-0.02}$	$0.51^{+0.08}_{-0.07}$	$0.91^{+0.15}_{-0.13}$	$0.50^{+0.06}_{-0.06}$	$0.89^{+0.11}_{-0.11}$	$0.59^{+0.06}_{-0.06}$	$1.1^{+0.11}_{-0.11}$	$0.60^{+0.16}_{-0.11}$	$1.10^{+0.29}_{-0.20}$
Ne	$1.42^{+0.10}_{-0.10}$	$1.49^{+0.64}_{-0.45}$	$1.1^{+0.46}_{-0.33}$	$1.39^{+0.30}_{-0.37}$	$0.98^{+0.22}_{-0.27}$	$0.64^{+0.29}_{-0.27}$	$0.45^{+0.21}_{-0.19}$	$2.1^{+0.68}_{-0.83}$	$1.5^{+0.49}_{-0.59}$
Mg	$0.42^{+0.06}_{-0.05}$	$0.33^{+0.20}_{-0.17}$	$0.79^{+0.49}_{-0.42}$	$0.31^{+0.20}_{-0.18}$	$0.74^{+0.49}_{-0.44}$	$0.34^{+0.14}_{-0.13}$	$0.81^{+0.35}_{-0.32}$	$0.78^{+0.74}_{-0.54}$	$1.9^{+1.8}_{-1.3}$
Si	$0.63^{+0.07}_{-0.06}$	$0.57^{+0.19}_{-0.16}$	$0.91^{+0.32}_{-0.27}$	$0.49^{+0.19}_{-0.17}$	$0.78^{+0.31}_{-0.28}$	$0.50^{+0.11}_{-0.10}$	$0.79^{+0.20}_{-0.18}$	$0.71^{+0.54}_{-0.44}$	$1.12^{+0.86}_{-0.71}$
S	$0.41^{+0.10}_{-0.10}$	1.0		1.0		$0.57^{+0.16}_{-0.16}$		1.0	

TESS and NICER were emitted as the ultimate result of a common physical phenomenon (e.g., nonthermal electrons). Previously, Osten & Wolk (2015) also found that, correcting for the fraction of the bolometric flare energy released in the different wave bands (coronal, optical), the optical FFD and coronal FFDs were consistent with each other, indicating a continuation of a common trend over a wide range of flare energies.

Since the Swift/UVOT flares U2, U7, and U8 were not observed for their full duration, the values of energies of those flares do not represent the total energies of corresponding flares. The largest energy (i.e., $\log E$ (erg) > 33.3, in Table 4) is not included in the FFD fit to reduce bias. The reported energy of flare U2, the next-largest flare, represents almost all the released energy since only a short part of U2's decay phase was not observed. Thus, we claim that the FFD of UVOT flares estimated in this paper is a good representation of flare rates even though the number of flares is small. Though we have a small number of UV flares, the shallower FFD slope matches the results of Mullan & Paudel (2018), who found that the FFD for a given star turns over to shallower slopes for low-energy flares in the $\log \tilde{\nu}$ versus $\log E$ diagram. For a slightly different flare energy range than that reported in this paper, Lacy et al. (1976) reported a value of $\beta = -0.69 \pm 0.11$ for EV Lac for U -band energies in the range $\log E_U \sim (30.5-32.5)$. However, they also included the energies of flares observed in other filters (B and V), which were converted to U -band energies. The value of β also depends on the range of flare energies used for fitting.

Audard et al. (2000) used *EUVE* data to study the distribution of coronal (EUV and X-ray) flare rates of EV Lac. They estimated $\beta = 0.76 \pm 0.33$, which matches well with our power-law fit to NICER X-ray flare energy distribution within $1-\sigma$. Likewise, Collura et al. (1988) estimated $\beta = 0.52$ for soft X-ray flares on M dwarfs by using *EXOSAT* data. Their results also agree with ours within 1σ .

6. Conclusions

In this work, we present simultaneous multiwavelength flare observations of the nearby, active M dwarf EV Lac. We obtained time series observations in the optical, UV, and X-ray, analyzed the star's flares in each band, and used these results to

compare the multiwavelength flare properties. Our major findings are:

1. TESS data reveal EV Lac has WLF rate of ~ 2 per day and a rotation period of 4.3592 days.
2. Swift UVOT observations indicate that EV Lac has a higher flare rate in the UV than in white light or X-ray, although this may be because the flares detected with UVOT are all of significantly smaller equivalent duration and energy than the TESS and NICER flares. The low-energy Swift UV flares also have larger amplitudes compared to the white light flares, likely because the flare emission peaks in the UV.
3. Our results (in Table 7) suggest that the flare luminosity in the optical is comparable to (or somewhat larger than) the flare luminosity in X-rays. This feature of flare radiation could be consistent with thermal processes of energy distribution (conduction, radiation) in flare plasma. This feature could also be consistent with bremsstrahlung emission from hot flare plasma (Andrews 1965; Mullan 1976b); see especially Kodaira (1977) for flares in EV Lac in particular. Bremsstrahlung emission extends at essentially constant flux at all frequencies that are less than $h\nu_{\max} \approx \text{kT}$. With $T = 3-30$ MK in flare plasma (see Table 5), such a spectrum could account for comparable energies radiated in ~ 1 keV X-rays and in optical light. However, it is not clear that a single mechanism can explain the various emissions that have been identified in stellar flares (Kowalski et al. 2013); these include a BB continuum with a temperature of order 10^4 K, emission in the Balmer continuum and in high-level Balmer lines, and a mysterious conundrum that appears at wavelengths redward of 6000 Å (possibly due to H-emission). Until such time as the contributions from these various components can be simultaneously quantified, it will be difficult to state definitively how flare energy is partitioned across the spectrum.
4. Given the uncertainties of the fitted abundances of four elements (O, Ne, Mg, and Si), the current study could not conclusively find evidence of the FIP nor the IFIP effect during the flares observed on EV Lac. Laming (2015) has proposed a model for generating the FIP and the IFIP in partially ionized plasmas, such as occur in the

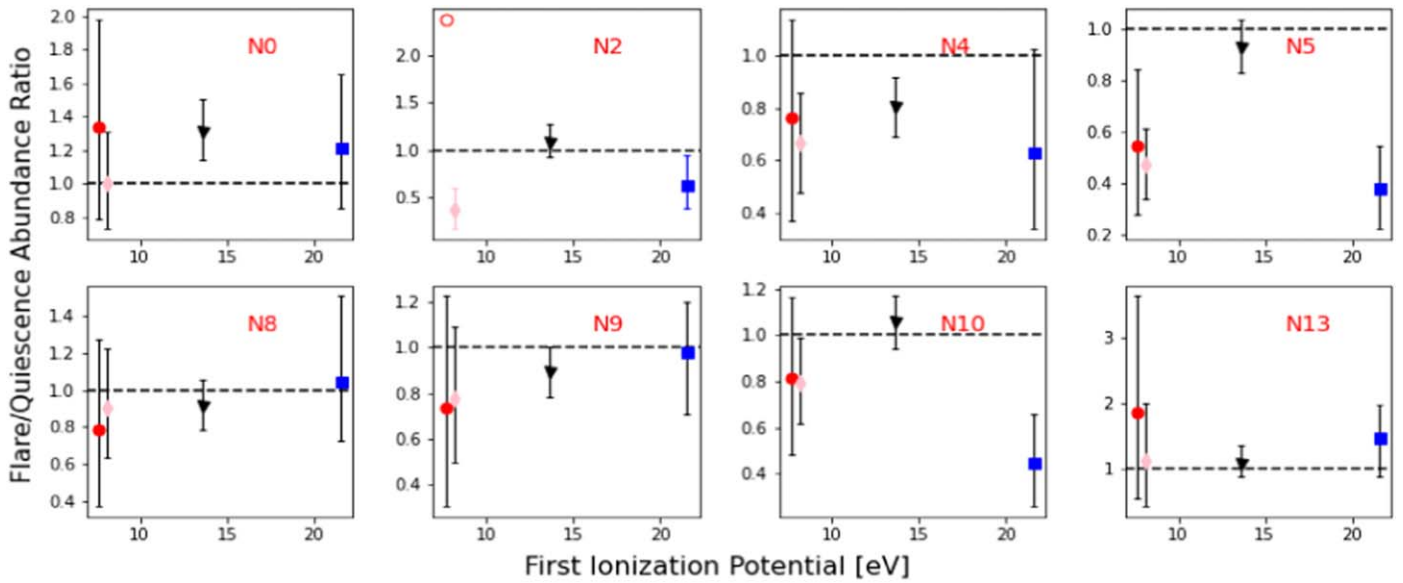


Figure 15. Flare abundance ratio for four elements: O, Ne, Mg, and Si, as a function of FIP. In each subplot, the red circle corresponds to Mg, the pink diamond corresponds to Si, the black triangle corresponds to O, and the blue square corresponds to Ne. The horizontal dashed line corresponds to the abundance ratio of the element during quiescent state of the star. A default value of 1.0 is used to estimate the ratio for Mg in the case of flare N2. Therefore, a hollow circle is used in the corresponding plot.

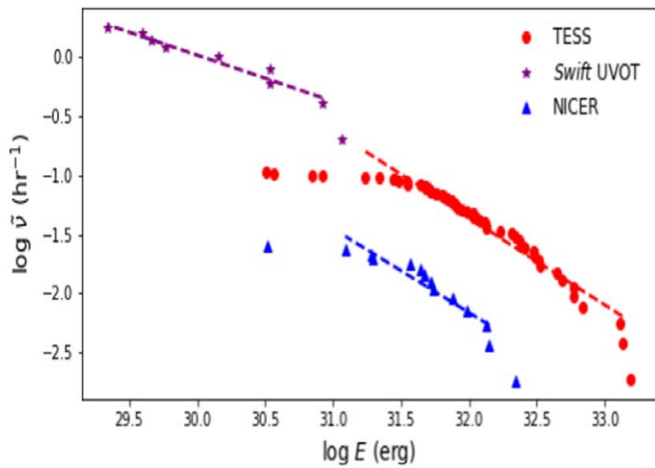


Figure 16. Comparison of FFDs of flares observed by TESS (red), NICER (blue), and Swift/UVOT (purple). Dashed lines show power-law fits to the distribution of flares in a given band.

Table 10
Power-law Fit to FFDs

Band	β	$\log E_{\min}$ erg	$\log E_{\max}$ erg	# of flares
TESS	-0.67 ± 0.09	31.2	33.1	51
Swift/UVOT	-0.38 ± 0.13	28.7	30.2	8
NICER	-0.65 ± 0.19	31.1	32.2	12

chromospheres of all cool stars. MHD waves propagating through the chromosphere exert a ponderomotive force on the ions but not (directly) on the neutrals, leading to ion-neutral fractionation. The fractionation has maximum amplitude at a certain altitude H (≈ 2150 km in the Sun). Laming shows that *upward*-propagating Alfvén waves favor the creation of the FIP effect, whereas downward-propagating fast-mode MHD waves favor the IFIP effect. Although the Sun in general displays the FIP effect in

active regions, transient detection of IFIP has been reported occasionally in localized regions during flares (Baker et al. 2019). The geometry of the field (closed or open field lines?) also contributes to the FIP/IFIP effect, as does the altitude H of predominant ion-neutral fractionation. The lack of an observed FIP or IFIP in EV Lac could be due to one or more of the following: (i) the presence of complicated field topology; (ii) a mixture of upward and downward wave fluxes; (iii) an unfavorable location of the altitude H .

In conclusion, our multiwavelength study of flares in one particular flare star (EV Lac) has helped to confirm certain aspects of how the radiant energy of flares is distributed across various regions of the electromagnetic spectrum. However, if it turns out that nonthermal electrons contain much of the flare energy (up to 50% in a sample of small solar flares; e.g., Lin & Hudson 1971), then it could be beneficial to include, in any future multiwavelength study of flares, observations of nonthermal X-rays. A flare-associated population of nonthermal electrons might, in principle, also be tracked by means of radio observations, and EV Lac is already known to emit circularly polarized flaring radiation at centimeter wavelengths (Osten et al. 2005). Unfortunately, Osten et al. reported that there seems to be no obvious relationship *in the timing* between the flares that they detected in centimeter radio, X-ray, or optical. In a joint optical-radio study of flaring stars, Spangler & Moffett (1976) reported a certain correlation in *timing* between the light curves in radio and optical: the radio peak at 318 MHz was found on average to be *delayed* by 0–5 minutes relative to the optical peak. If this time delay in the light curves is related to physical processes in the flare and/or in the corona, then future multiwavelength campaigns could benefit from the use of meter-wave radio data.

The material in this paper is based upon work supported by NASA under award No. 80NSSC19K0104, 80NSSC19K0315 and 80GSFC21M0002. L.D.V. acknowledges funding support from the Heising-Simons Astrophysics

Postdoctoral Launch Program, through a grant to Vanderbilt University. D.H. acknowledges support from the Alfred P. Sloan Foundation, the National Aeronautics and Space Administration (80NSSC19K0379), and the National Science Foundation (AST-1717000). M.A.T. acknowledges support from the DOE CSGF program through grant DE-SC0019323. This paper includes data collected by the TESS mission. Funding for the TESS mission is provided by the NASA Explorer Program. This work made use of data supplied by the UKSSDC at the University of Leicester. This research has made use of the XRT Data Analysis Software developed under the responsibility of the ASI Science Data Center, Italy. This work makes use of observations from the LCOGT network. This research has made use of data obtained through the High Energy Astrophysics Science Archive Research Center Online Service, provided by the NASA/Goddard Space Flight Center. This publication makes use of data products from the Wide-field Infrared Survey Explorer, which is a joint project of the University of California, Los Angeles, and the Jet Propulsion Laboratory/California Institute of Technology, funded by the National Aeronautics and Space Administration. This publication makes use of data products from the Two Micron All Sky Survey, which is a joint project of the University of Massachusetts and the Infrared Processing and Analysis Center/California Institute of Technology, funded by the National Aeronautics and Space Administration and the National Science Foundation. This research made use of Photutils, an Astropy package for detection and photometry of astronomical sources.




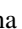



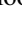

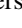





The authors wish to recognize and acknowledge the very significant cultural role and reverence that the summit of Maunakea has always had within the indigenous Hawaiian community. We are most fortunate to have the opportunity to conduct observations from this mountain.

Software: Astropy (Astropy Collaboration et al. 2013, 2018), Matplotlib (Hunter 2007), Numpy (Harris et al. 2020), Lightkurve (Vinícius et al. 2018), Python, IPython Perez & Granger (2007), Jupyter (Kluyver et al. 2016).

Facility: TESS, Swift XRT/UVOT, NICER.

University of Hawaii 2.2-meter Telescope (UH88), Las Cumbres Observatory Global Telescope (LCOGT).

ORCID iDs

Rishi R. Paudel  <https://orcid.org/0000-0002-8090-3570>
 Thomas Barclay  <https://orcid.org/0000-0001-7139-2724>
 Joshua E. Schlieder  <https://orcid.org/0000-0001-5347-7062>
 Elisa V. Quintana  <https://orcid.org/0000-0003-1309-2904>
 Emily A. Gilbert  <https://orcid.org/0000-0002-0388-8004>
 Laura D. Vega  <https://orcid.org/0000-0002-5928-2685>
 Allison Youngblood  <https://orcid.org/0000-0002-1176-3391>
 Michele L. Silverstein  <https://orcid.org/0000-0003-2565-7909>
 Rachel A. Osten  <https://orcid.org/0000-0001-5643-8421>
 Michael A. Tucker  <https://orcid.org/0000-0002-2471-8442>
 Daniel Huber  <https://orcid.org/0000-0001-8832-4488>
 Aaron Do  <https://orcid.org/0000-0003-3429-7845>
 Kenji Hamaguchi  <https://orcid.org/0000-0001-7515-2779>
 D. J. Mullan  <https://orcid.org/0000-0002-7087-9167>
 John E. Gizis  <https://orcid.org/0000-0002-8916-1972>
 Teresa A. Monsue  <https://orcid.org/0000-0003-3896-3059>

Knicole D. Colón  <https://orcid.org/0000-0001-8020-7121>
 Patricia T. Boyd  <https://orcid.org/0000-0003-0442-4284>
 James R. A. Davenport  <https://orcid.org/0000-0002-0637-835X>
 Lucianne Walkowicz  <https://orcid.org/0000-0003-2918-8687>

References

- Abdul-Aziz, H., Abranin, E. P., Alekseev, I. Y., et al. 1995, *A&AS*, **114**, 509
 Allard, F., Homeier, D., & Freytag, B. 2012, *RSPTA*, **370**, 2765
 Ambruster, C. W., Pettersen, B. R., Hawley, S., Coleman, L. A., & Sandmann, W. H. 1986, ESA Special Publication, New Insights in Astrophysics. Eight Years of UV Astronomy with IUE, Vol. 263 ed. E. J. Rolfe & R. Wilson, 137
 Anders, E., & Grevesse, N. 1989, *Geochim. Cosmochim. Acta*, **53**, 197
 Andrews, A. D. 1965, *IrAJ*, **7**, 20
 Arnaud, K. A. 1996, in ASP Conf. Ser. 101, XSPEC: The First Ten Years, ed. G. H. Jacoby & J. Barnes (San Francisco, CA: ASP), 17
 Astropy Collaboration, Price-Whelan, A. M., Sipőcz, B. M., et al. 2018, *AJ*, **156**, 123
 Astropy Collaboration, Robitaille, T. P., Tollerud, E. J., et al. 2013, *A&A*, **558**, A33
 Audard, M., Güdel, M., Drake, J. J., & Kashyap, V. L. 2000, *ApJ*, **541**, 396
 Audard, M., Güdel, M., & Mewe, R. 2001, *A&A*, **365**, L318
 Bacon, R., Copin, Y., Monnet, G., et al. 2001, *MNRAS*, **326**, 23
 Bailer-Jones, C. A. L., Rybizki, J., Fouesneau, M., Mantelet, G., & Andrae, R. 2018, *AJ*, **156**, 58
 Baker, D., van Driel-Gesztelyi, L., Brooks, D. H., et al. 2019, *ApJ*, **875**, 35
 Ballard, S. 2019, *AJ*, **157**, 113
 Barclay, T., & Gilbert, E. 2020, mrtommyb/xoflares, v0.2.1, Zenodo, doi:10.5281/zenodo.4156285
 Barclay, T., Pepper, J., & Quintana, E. V. 2018, *ApJS*, **239**, 2
 Benedict, G. F., Henry, T. J., Franz, O. G., et al. 2016, *AJ*, **152**, 141
 Benz, A. O., & Güdel, M. 2010, *ARA&A*, **48**, 241
 Bessell, M. S., Castelli, F., & Plez, B. 1998, *A&A*, **333**, 231
 Boller, T., Freyberg, M. J., Trümper, J., et al. 2016, *A&A*, **588**, A103
 Bolmont, E., Selsis, F., Owen, J. E., et al. 2017, *MNRAS*, **464**, 3728
 Borucki, W. J. 2017, *PAPhS*, **161**, 38
 Bowler, B. P., Liu, M. C., Shkolnik, E. L., et al. 2012, *ApJ*, **753**, 142
 Bradley, L., Sipocz, B., Robitaille, T., et al. 2016, Photutils: Photometry tools, ascl:1609.011
 Brandt, T. D., & Huang, C. X. 2015a, *ApJ*, **807**, 24
 Brandt, T. D., & Huang, C. X. 2015b, *ApJ*, **807**, 58
 Brinkman, A. C., Behar, E., Güdel, M., et al. 2001, *A&A*, **365**, L324
 Broomhall, A.-M., Davenport, J. R. A., Hayes, L. A., et al. 2019, *ApJS*, **244**, 44
 Burrows, A., Hubbard, W. B., Lunine, J. I., & Liebert, J. 2001, *RvMP*, **73**, 719
 Burrows, D. N., Hill, J. E., Nousek, J. A., et al. 2005, *SSRv*, **120**, 165
 Buton, C., Copin, Y., Aldering, G., et al. 2013, *A&A*, **549**, A8
 Chambers, K. C., Magnier, E. A., Metcalfe, N., et al. 2016, arXiv:1612.05560
 Chen, H., Zhan, Z., Youngblood, A., et al. 2021, *NatAs*, **5**, 298
 Chen, P. F., & Priest, E. R. 2006, *SoPh*, **238**, 313
 Collura, A., Pasquini, L., & Schmitt, J. H. M. M. 1988, *A&A*, **205**, 197
 Cram, L. E., & Woods, D. T. 1982, *ApJ*, **257**, 269
 Curtis, J. L., Agüeros, M. A., Matt, S. P., et al. 2020, *ApJ*, **904**, 140
 Cutri, R. M., Skrutskie, M. F., van Dyk, S., et al. 2003, *yCat*, **2246**, 0
 Cutri, R. M., et al. 2012, *yCat*, **2311**, 0
 Dahm, S. E. 2015, *ApJ*, **813**, 108
 Davenport, J. R. A. 2016, *ApJ*, **829**, 23
 Dieterich, S. B., Henry, T. J., Jao, W.-C., et al. 2014, *AJ*, **147**, 94
 Douglas, S. T., Agüeros, M. A., Covey, K. R., & Kraus, A. 2017, *ApJ*, **842**, 83
 Douglas, S. T., Curtis, J. L., Agüeros, M. A., et al. 2019, *ApJ*, **879**, 100
 Engle, S. G., & Guinan, E. F. 2018, *RNAAS*, **2**, 34
 Favata, F., Reale, F., Micela, G., et al. 2000, *A&A*, **353**, 987
 Feldman, U. 1992, *PhysS*, **46**, 202
 Foreman-Mackey, D. 2018, *RNAAS*, **2**, 31
 Foreman-Mackey, D., Agol, E., Ambikasaran, S., & Angus, R. 2017, *AJ*, **154**, 220
 France, K., Duvvuri, G., Egan, H., et al. 2020, *AJ*, **160**, 237
 France, K., Loyd, R. O. P., Youngblood, A., et al. 2016, *ApJ*, **820**, 89
 Gagné, J., Mamajek, E. E., Malo, L., et al. 2018, *ApJ*, **856**, 23
 Gaia Collaboration, Babusiaux, C., van Leeuwen, F., et al. 2018b, *A&A*, **616**, A10
 Gaia Collaboration, Brown, A. G. A., Vallenari, A., et al. arXiv:1804.09365

- Gendreau, K. C., Arzoumanian, Z., Adkins, P. W., et al. 2016, *Proc. SPIE*, **9905**, 99051H
- Gershberg, R. E. 1972, *Ap&SS*, **19**, 75
- Gershberg, R. E. 2005, *Solar-Type Activity in Main-Sequence Stars* (Berlin: Springer)
- Güdel, M., Audard, M., Reale, F., Skinner, S. L., & Linsky, J. L. 2004, *A&A*, **416**, 713
- Güdel, M., Linsky, J. L., Brown, A., & Nagase, F. 1999, *ApJ*, **511**, 405
- Harris, C. R., Millman, K. J., van der Walt, S. J., et al. 2020, *Natur*, **585**, 357
- Hawley, S. L., Gizis, J. E., & Reid, I. N. 1996, *AJ*, **112**, 2799
- Henry, T. J., Jao, W.-C., Subasavage, J. P., et al. 2006, *AJ*, **132**, 2360
- Houdebine, E. R., Mullan, D. J., Bercu, B., Paletou, F., & Gebran, M. 2017, *ApJ*, **837**, 96
- Huenemoerder, D. P., Schulz, N. S., Testa, P., et al. 2010, *ApJ*, **723**, 1558
- Hünsch, M., Schmitt, J. H. M. M., Sterzik, M. F., & Voges, W. 1999, *A&S*, **135**, 319
- Hunter, J. D. 2007, *CSE*, **9**, 90
- Inglis, A. R., Ireland, J., Dennis, B. R., Hayes, L., & Gallagher, P. 2016, *ApJ*, **833**, 284
- Jackman, J. A. G., Wheatley, P. J., Pugh, C. E., et al. 2019, *MNRAS*, **482**, 5553
- Johns-Krull, C. M., & Valenti, J. A. 1996, *ApJL*, **459**, L95
- Johnson, D. R. H., & Soderblom, D. R. 1987, *AJ*, **93**, 864
- Jones, J., White, R. J., Boyajian, T., et al. 2015, *ApJ*, **813**, 58
- King, J. R., Villarreal, A. R., Soderblom, D. R., Gulliver, A. F., & Adelman, S. J. 2003, *AJ*, **125**, 1980
- Klutsch, A., Freire Ferrero, R., Guillout, P., et al. 2014, *A&A*, **567**, A52
- Kluyver, T., Ragan-Kelley, B., Pérez, F., et al. 2016, in *Positioning and Power in Academic Publishing: Players, Agents and Agendas*, ed. F. Loizides & B. Schmidt (Amsterdam: IOS Press), 87
- Kodaira, K. 1977, *A&A*, **61**, 625
- Kodaira, K., Ichimura, K., & Nishimura, S. 1976, *PASJ*, **28**, 665
- Kopparapu, R. K., Ramirez, R., Kasting, J. F., et al. 2013, *ApJ*, **765**, 131
- Kowalski, A. F., Hawley, S. L., Wisniewski, J. P., et al. 2013, *ApJS*, **207**, 15
- Kucukelbir, A., Tran, D., Ranganath, R., Gelman, A., & Blei, D. M. 2016, arXiv:1603.00788
- Kupriyanova, E. G., Melnikov, V. F., Puzynya, V. M., Shibasaki, K., & Ji, H. S. 2014, *ARep*, **58**, 573
- Lacy, C. H., Moffett, T. J., & Evans, D. S. 1976, *ApJS*, **30**, 85
- Lalitha, S. 2016, in *IAU Symp. 320, Solar and Stellar Flares and their Effects on Planets*, ed. A. G. Kosovichev, S. L. Hawley, & P. Heinzel (Cambridge: Cambridge University Press), 155
- Laming, J. M. 2015, *LRSP*, **12**, 2
- Lammer, H., Lichtenegger, H. I. M., Kulikov, Y. N., et al. 2007, *AsBio*, **7**, 185
- Lantz, B., Aldering, G., Antilogus, P., et al. 2004, *Proc. SPIE*, **5249**, 146
- Lin, R. P., & Hudson, H. S. 1971, *SoPh*, **17**, 412
- Loyd, R. O. P., France, K., Youngblood, A., et al. 2018b, *ApJ*, **867**, 71
- Loyd, R. O. P., Shkolnik, E. L., Schneider, A. C., et al. 2018a, *ApJ*, **867**, 70
- Mamajek, E. E. 2010, *AAS Meeting*, 215, 455.05
- Mann, A. W., Feiden, G. A., Gaidos, E., Boyajian, T., & von Braun, K. 2015, *ApJ*, **804**, 64
- McCully, C., Turner, M., Volgenau, N., et al. 2018, *Zenodo*, 1257560
- Melbourne, K., Youngblood, A., France, K., et al. 2020, *AJ*, **160**, 269
- Morin, J., Donati, J. F., Petit, P., et al. 2008, *MNRAS*, **390**, 567
- Mullan, D. J. 1976a, *ApJ*, **207**, 289
- Mullan, D. J. 1976b, *ApJ*, **210**, 702
- Mullan, D. J., & Bais, H. P. 2018, *ApJ*, **865**, 101
- Mullan, D. J., & Paudel, R. R. 2018, *ApJ*, **854**, 14
- Nakariakov, V. M., Foullon, C., Verwichte, E., & Young, N. P. 2006, *A&A*, **452**, 343
- Nakariakov, V. M., Pilipenko, V., Heilig, B., et al. 2016, *SSRv*, **200**, 75
- Newton, E. R., Irwin, J., Charbonneau, D., et al. 2017, *ApJ*, **834**, 85
- Osten, R. A., Ayres, T. R., Brown, A., Linsky, J. L., & Krishnamurthi, A. 2003, *ApJ*, **582**, 1073
- Osten, R. A., Godet, O., Drake, S., et al. 2010, *ApJ*, **721**, 785
- Osten, R. A., Hawley, S. L., Allred, J., et al. 2006, *ApJ*, **647**, 1349
- Osten, R. A., Hawley, S. L., Allred, J. C., Johns-Krull, C. M., & Roark, C. 2005, *ApJ*, **621**, 398
- Osten, R. A., Kowalski, A., Drake, S. A., et al. 2016, *ApJ*, **832**, 174
- Osten, R. A., & Wolk, S. J. 2015, *ApJ*, **809**, 79
- Paudel, R. R., Gizis, J. E., Mullan, D. J., et al. 2018a, *ApJ*, **858**, 55
- Paudel, R. R., Gizis, J. E., Mullan, D. J., et al. 2018b, *ApJ*, **861**, 76
- Pecaut, M. J., & Mamajek, E. E. 2013, *ApJS*, **208**, 9
- Perez, F., & Granger, B. E. 2007, *CSE*, **9**, 21
- Pettersen, B. R. 1980, *AJ*, **85**, 871
- Pitkin, M., Williams, D., Fletcher, L., & Grant, S. D. T. 2014, *MNRAS*, **445**, 2268
- Pollacco, D. L., Skillen, I., Collier Cameron, A., et al. 2006, *PASP*, **118**, 1407
- Pomerance, B. H., Abbott, B., & Ambruster, C. 1995, *AAS Meeting*, 186, 21.03
- Proctor, R. A. 1869, *RSPS*, **18**, 169
- Pugh, C. E., Armstrong, D. J., Nakariakov, V. M., & Broomhall, A. M. 2016, *MNRAS*, **459**, 3659
- Raassen, A. J. J., Mewe, R., Audard, M., & Güdel, M. 2003, *A&A*, **411**, 509
- Raassen, A. J. J., Mitra-Kraev, U., & Güdel, M. 2007, *MNRAS*, **379**, 1075
- Ranjan, S., Wordsworth, R., & Sasselov, D. D. 2017, *ApJ*, **843**, 110
- Reid, I. N., Hawley, S. L., & Gizis, J. E. 1995, *AJ*, **110**, 1838
- Reiners, A., Zechmeister, M., Caballero, J. A., et al. 2018, *A&A*, **612**, A49
- Ribas, I., Bolmont, E., Selsis, F., et al. 2016, *A&A*, **596**, A111
- Ricker, G. R. 2014, *JAVSO*, **42**, 234
- Ricker, G. R. 2015, *AAS Meeting*, 47, 503.01, *AAS/Division for Extreme Solar Systems Abstracts*
- Rojas-Ayala, B., Covey, K. R., Muirhead, P. S., & Lloyd, J. P. 2012, *ApJ*, **748**, 93
- Roman, N. G. 1949, *ApJ*, **110**, 205
- Roming, P. W. A., Kennedy, T. E., Mason, K. O., et al. 2005, *SSRv*, **120**, 95
- Roques, P. E. 1955, *PASP*, **67**, 34
- Saar, S. H. 1994, in *Invited Papers from IAU Coll. 143: The Sun as a Variable Star: Solar and Stellar Irradiance Variations*, ed. J. M. Pap et al. (Cambridge: Cambridge University Press), 147
- Salvatier, J., Wiecki, T. V., & Fonnesbeck, C. 2016, *PeerJ Computer Science*, **2**, e55
- Schlieder, J. E., Skemer, A. J., Maire, A.-L., et al. 2016, *ApJ*, **818**, 1
- Schmidt, S. J., Prieto, J. L., Stanek, K. Z., et al. 2014, *ApJL*, **781**, L24
- Schmitt, J. H. M. M. 1994, *ApJS*, **90**, 735
- Schmitt, J. H. M. M., Fleming, T. A., & Giampapa, M. S. 1995, *ApJ*, **450**, 392
- Schmitt, J. H. M. M., Ioannidis, P., Robrade, J., Czesla, S., & Schneider, P. C. 2019, *A&A*, **628**, A79
- Schrijver, C. J., Bagenal, F., & Sojka, J. J. 2016, *Heliophysics: Active Stars, their Atmospheres, and Impacts on Planetary Environments* (Cambridge: Cambridge University Press)
- Sciortino, S., Maggio, A., Favata, F., & Orlando, S. 1999, *A&A*, **342**, 502
- Segura, A., Walkowicz, L. M., Meadows, V., Kasting, J., & Hawley, S. 2010, *AsBio*, **10**, 751
- Shkolnik, E. L., Anglada-Escudé, G., Liu, M. C., et al. 2012, *ApJ*, **758**, 56
- Shkolnik, E. L., & Barman, T. S. 2014, *AJ*, **148**, 64
- Shporer, A., Brown, T., Lister, T., et al. 2011, in *The Astrophysics of Planetary Systems: Formation, Structure, and Dynamical Evolution*, ed. A. Sozzetti, M. G. Lattanzi, & A. P. Boss, Vol. 276 (Cambridge: Cambridge University Press), 553
- Shulyak, D., Reiners, A., Engeln, A., et al. 2017, *NatAs*, **1**, 0184
- Smith, R. K., Brickhouse, N. S., Liedahl, D. A., & Raymond, J. C. 2001, *ApJL*, **556**, L91
- Spangler, S. R., & Moffett, T. J. 1976, *ApJ*, **203**, 497
- Stassun, K. G., Oelkers, R. J., Pepper, J., et al. 2018, *AJ*, **156**, 102
- Stauffer, J. R., Schultz, G., & Kirkpatrick, J. D. 1998, *ApJL*, **499**, L199
- Tilley, M. A., Segura, A., Meadows, V., Hawley, S., & Davenport, J. 2019, *AsBio*, **19**, 64
- Tonry, J. L., Denneau, L., Flewelling, H., et al. 2018, *ApJ*, **867**, 105
- Van Doorselaere, T., Kupriyanova, E. G., & Yuan, D. 2016, *SoPh*, **291**, 3143
- Vida, K., Oláh, K., Kóvári, Z., et al. 2019, *ApJ*, **884**, 160
- Vinícius, Z., Barentsen, G., Hedges, C., Gully-Santiago, M., & Cody, A. M. 2018, *Zenodo*, 1181928
- Weis, E. W. 1996, *AJ*, **112**, 2300
- White, S. M., Jackson, P. D., & Kundu, M. R. 1989, *ApJS*, **71**, 895
- Wright, E. L., Eisenhardt, P. R. M., Mainzer, A. K., et al. 2010, *AJ*, **140**, 1868
- Yamada, S., Axelsson, M., Ishisaki, Y., et al. 2019, *PASJ*, **71**, 75
- Youngblood, A., France, K., Loyd, R. O. P., et al. 2017, *ApJ*, **843**, 31
- Zacharias, N., Finch, C. T., Girard, T. M., et al. 2012, *yCat*, **1322**, 0
- Zacharias, N., Finch, C. T., Girard, T. M., et al. 2013, *AJ*, **145**, 44
- Zaitsev, V. V., & Stepanov, A. V. 1982, *SvAL*, **8**, 132